



HAL
open science

Plastic deformation and trace element mobility in sphalerite

Alexandre Cugerone, Emilien Oliot, Manuel Munoz, Fabrice Barou, Vincent Motto- Ros, Bénédicte Cenki

► **To cite this version:**

Alexandre Cugerone, Emilien Oliot, Manuel Munoz, Fabrice Barou, Vincent Motto- Ros, et al.. Plastic deformation and trace element mobility in sphalerite. *The American Mineralogist*, In press, 10.2138/am-2023-9215 . hal-04532279

HAL Id: hal-04532279

<https://hal.science/hal-04532279>

Submitted on 4 Apr 2024

HAL is a multi-disciplinary open access archive for the deposit and dissemination of scientific research documents, whether they are published or not. The documents may come from teaching and research institutions in France or abroad, or from public or private research centers.

L'archive ouverte pluridisciplinaire **HAL**, est destinée au dépôt et à la diffusion de documents scientifiques de niveau recherche, publiés ou non, émanant des établissements d'enseignement et de recherche français ou étrangers, des laboratoires publics ou privés.

1 Review 1

2 **Plastic deformation and trace element mobility in**
3 **sphalerite**

4 Word count (without reference list and captions): 9644

5

6

7 **Alexandre Cugerone^{1,2}, Emilien Oliot², Manuel Munoz², Fabrice Barou², Vincent Motto-**
8 **Ros³, Bénédicte Cenki²**

9 ¹Department of Earth Sciences, University of Geneva, Geneva, Switzerland;

10 alexandre.cugerone@unige.ch

11 ²Géosciences Montpellier, Université de Montpellier, France ; emilien.oliot@umontpellier.fr;

12 manuel.munoz@umontpellier.fr; fabrice.barou@umontpellier.fr;

13 benedicte.cenki@umontpellier.fr

14 ³Institut Lumière Matière Université Lyon 1, France ; vincent.motto-ros@univ-lyon1.fr

15

16

17

18

19

Abstract

20 Sphalerite (ZnS) is a sulfide found in a large variety of ore deposits and is frequently
21 hosted in metamorphic terranes that have undergone deformation and related recrystallization.
22 However, deformation mechanisms of sphalerite are still poorly understood because
23 recrystallization evidence is barely visible under the optical microscope and may reflect
24 complex and frequently multistage mechanisms. Furthermore, sphalerite may host up to a few
25 thousands ppm of critical metals such as gallium (Ga), germanium (Ge), and indium (In).
26 Metamorphic conditions and dynamic recrystallization may have induced local or total
27 redistribution of these elements. Modern techniques such as electron backscattered diffraction
28 analyses (EBSD) and laser induced breakdown spectroscopy (LIBS) applied on sphalerite
29 allow to detect grain boundaries, crystal-plastic deformation and internal chemical diffusion,
30 which classically reflect active deformation mechanisms. In this study, a microstructural and
31 in-situ chemical comparison between four sphalerite types (type i, ii, iii, iv) is made for the
32 first time. The four sphalerite types present different deformation imprints although they are
33 hosted in a similar geological setting: the Pyrenean Axial Zone and the Montagne Noire
34 Variscan massifs (France). Based on EBSD and LIBS mapping, we describe two regional
35 sphalerite growth stages composed of dark red crystals with polygonal shape (type i;
36 Bentaillou-Liat deposit) and light to dark-brown euhedral crystals (type iii; Saint Salvy
37 deposit). New investigation at microscale on sphalerite grains from the Saint-Salvy deposit
38 shows late Cu-Ge-Ga enrichment not only in specific sector zonings, but also in grain
39 boundaries, growing crystal edges and in low angle misorientation or twin boundaries.
40 Following a deformation event that probably occurred during the Pyrenean-Alpine orogeny,
41 these two sphalerite mineralizations have both endured plastic deformation in a dislocation
42 creep regime and dynamically recovered by subgrain rotation (SGR) mechanism. Two
43 mechanisms of Cu-Ga-Ge spatial redistribution are observed and are key processes for the

44 crystallization of Cu-Ga-Ge-rich minerals in sphalerite veins. The first mechanism involved
45 the in-situ redistribution of Cu-Ga-Ge contents from a pre-existing concentration in the
46 sphalerite lattice (type iii, Arre deposit), creating Ge-sulfides (briartite), probably during
47 Pyrenean-Alpine orogeny. Formation of this type of Ge-mineral may be related to solid-state
48 diffusion processes. The second mechanism is associated with the circulation of a Cu-Ga-Ge-
49 rich fluid in surrounding rocks. In the pre-existing polygonal sphalerite from Late-Variscan
50 veins (type ii, Pale Bidau deposit), millimeter size bands of small (<50 μm), recrystallized
51 sphalerite grains are locally observed. Thos domains contain inclusions of Cu (chalcopyrite),
52 Ga and Ge minerals (brunogeierite, carboirite). Fluid-induced diffusion in the polygonal
53 sphalerite aggregates may occur with superimposed dynamic recrystallization, such as the
54 Late-Variscan veins (type ii, Pale Bidau-type). During post-Variscan time, this fluid enriched
55 in Cu-Ga-Ge largely circulated in the upper-crust of this Variscan terrane. This study
56 highlights the key importance of coupled textural (EBSD analyses) and in-situ chemical
57 analyses (LIBS mapping) of diverse sphalerite types at regional scale in order to indirectly
58 unravel the origin of vein mineralization, and their related critical metal distribution.

59

1. Introduction

60 Sphalerite is a base metal sulfide extensively mined for zinc (Zn) that frequently hosts
61 by-products such as germanium (Ge), gallium (Ga) and indium (In), considered as critical
62 metals by the U.S (U.S. Geological Survey. 2019) and the E.U. (European Commission.
63 2020). The largest volumes of sphalerite are reported in sediment-hosted and volcanogenic
64 massive sulfide ore deposits (SHMS and VHMS) that are frequently documented in deformed
65 and metamorphosed geological environments. In this case, sphalerite may show evidence of
66 dynamic recrystallization with frequent “core-mantle” recrystallized texture and/or static
67 recrystallization with textures made of coarse equant polygonal grains (Gilligan and Marshall
68 1987; Plimer 1987; Wagner and Cook 1998; Vikentyev et al. 2016; Cugerone et al. 2020).

69 Observations on both naturally and experimentally deformed sphalerite samples
70 revealed that, at low-grade conditions (< 400 °C, 200-500 MPa) crystal-plastic deformation
71 and dynamic recrystallization of sphalerite occur, demonstrating the relative softness of
72 sphalerite compared to other sulfide minerals such as pyrite and gangue minerals such as
73 quartz (Stanton and Gorman 1968; Gill 1969; Clark and Kelly 1973a; Siemes and Borges
74 1979; Siemes and Hennig-Michaeli 1985; Pesquera and Velasco 1993). Before the emergence
75 of modern microstructural mapping techniques such as electron back-scattered diffraction
76 (EBSD), only a few experimental works have described sphalerite deformation mechanisms
77 such as translation gliding and twin gliding parallel to {111} planes (Siemes et al. 1973) and
78 the presence of deformation-twinning during axial compression between 450 to 600 °C at 300
79 MPa (Couderc et al. 1985).

80 Identifying the mode of plastic deformation and recrystallization in sphalerite is essential
81 because these mechanisms may affect its critical metal contents (Ge, Ga, In, Cd; Cugerone et
82 al. 2020). In weakly deformed environments, critical metals such as Ge, Ga, In are frequently
83 considered to be incorporated in the sphalerite lattice (Bélissont et al. 2014; Frenzel et al.

84 2016; Bauer et al. 2019). These critical metals may be hosted in specific domains in
85 sphalerite, such as oscillatory bands (colloform layers; Luo et al. 2022; Sun et al. 2023)
86 associated with acicular crystals. Or they may be concentrated in euhedral crystals with
87 internal zones such as rhythmic bands with angular and straight geometry and sector zones
88 with general triangular or trapezoidal shape (Di Benedetto et al. 2005; Bélistont et al. 2014).
89 One particularly well-studied example of weakly deformed sphalerite is from the Saint Salvy
90 deposit (Johan 1988; Bélistont et al. 2016), where coarse millimeter size crystals are zoned
91 with light to dark brown rhythmic bands and sector zones. The sector zones are richer in Cu,
92 Ge and Ga (up to 7440 ppm Cu, 2500 ppm Ge and 1054 ppm Ga) than the rhythmic bands (up
93 to 4074 ppm Cu, 340 ppm Ge and 919 ppm Ga; Bélistont et al. 2014). This type of sphalerite
94 has formed in a low temperature hydrothermal environment (< 150°C; Munoz et al. 1994) and
95 shows relatively poor In contents (< 100 ppm In; Bélistont et al. 2014). In the sphalerite
96 lattice, Ga and Ge incorporation is well known and commonly associated with two
97 substitution mechanisms correlated with Cu and or Ag: $3\text{Zn}^{2+} \leftrightarrow \text{Ge}^{4+} + 2(\text{Cu}, \text{Ag})^{+}$ and
98 $3\text{Zn}^{2+} \leftrightarrow \text{Ga}^{3+} + \text{Cu}^{+}$ (Johan 1988; Cook et al. 2009; Ye et al. 2011; Bélistont et al. 2014;
99 George et al. 2016; Bauer et al. 2019; Fougrouse et al. 2023). However, plastic deformation
100 of sphalerite and metamorphic processes may redistribute Cu, Ga, Ge, involving the new
101 formation of nano to micro Cu(-Ga)-Ge minerals as shown by Cugerone et al. (2020).
102 Nonetheless, despite recent studies on the impact of recrystallization on sphalerite
103 (Lockington et al. 2014; George et al. 2016; Cugerone et al. 2020; Paradis et al. 2023), the
104 link between metamorphic imprint coupled to trace element distribution in sphalerite is still
105 poorly understood. Complex textures and heterogeneous chemical distributions at micro- to
106 nanoscale is commonly observed in these deformed systems, and the use of EBSD technique
107 and trace element mapping, from micro to nanoscale is key before making interpretation for
108 the incorporation mechanism in sphalerite (Fougrouse et al. 2023).

109 In this study, we have selected four types of sphalerite displaying variable degrees of
110 deformation, from weakly deformed to fully recrystallized. These sphalerite types are located
111 in two similar geological settings hosted in the Variscan Pyrenean Axial Zone and Montagne-
112 Noire (Saint-Salvy deposit). Similarities in their genesis and chemical contents between Saint-
113 Salvy and Pyrenean sphalerite allow to consider the Saint-Salvy sphalerite as a reference
114 sphalerite, which did not record an important deformation and metamorphic imprint (Johan
115 1988; BéliSSont et al. 2014, 2016). The EBSD method was used to map grains textures and
116 analyze crystallographic orientations of four types of sphalerite from the two main Pb-Zn
117 mineralizing events reported in the South of France (Variscan and post-Variscan). Coupled to
118 EBSD analyses, laser-induced breakdown spectroscopy (LIBS) chemical maps illustrate the
119 intertwined associations between microstructures and trace element (Cu, Ga, Ge) distribution
120 at microscale to explain the chemical mechanisms and their relationships with deformation
121 and metamorphism.

122 **2. Geological setting and sphalerite types**

123 **presentation**

124 The studied Pb-Zn deposits are hosted in the Paleozoic basement of the Montagne Noire
125 (MN; South of the Massif Central) and the Pyrenean Axial Zone (PAZ; including Basque
126 massifs; Figs. 1A and 1B) which are mostly composed of Paleozoic metasedimentary rocks,
127 Ordovician gneiss, and Carboniferous granites (Fig. 1B). During the Variscan orogeny
128 (Carboniferous- to Early-Permian), deformation and metamorphism involved the formation of
129 a main foliation (S1) and a cleavage (S2) in Pre-Carboniferous rocks (Zwart 1963; Mezger
130 and Gerdes 2016; Trap et al. 2017). Following the Variscan orogeny, a long period of
131 Mesozoic lithospheric extension occurred until Early-Cretaceous times (Clerc et al. 2015).
132 Between Late-Cretaceous and Miocene times, a second tectonic inversion period,

133 corresponding to the Cenozoic Pyrenean-Alpine orogeny, is generally recognized close to
134 regional-scale thrusts and faults, with limited extension and imprint on the surrounded rocks
135 (Cochelin et al. 2017).

136 In Western Europe, a large number of Pb-Zn stratabound and crosscutting vein
137 deposits are reported in the Variscan basement and the Mesozoic sedimentary cover. They
138 host significant amounts of Ge, Ga and In in sphalerite (Bélissont et al. 2014; Bauer et al.
139 2017; Walter et al. 2018). In these massifs (Fig. 1B), sphalerite veins generally formed at low-
140 to medium-temperatures (100-300 °C) and are associated with two
141 hydrothermal/metamorphic periods: (i) Variscan Pb-Zn stage is related to the end of the
142 widespread Variscan magmatism and metamorphism (Cugerone et al. 2021b); (ii) Post-
143 Variscan Pb-Zn stage is commonly associated with vast extension periods and fluid
144 migration(s) along unconformities (Mucchez et al. 2005; Cathelineau et al. 2012; Bons et al.
145 2014).

146 In Variscan terranes of the MN massif and the PAZ (Fig. 1B), Pb-Zn mineralizations
147 are similarly composed of two mineralizing stages (Variscan and post-Variscan). Four
148 sphalerite types can be described:

149 Type (i) sphalerite is part of the epigenetic stratabound stage and is synchronous to the
150 main Variscan magmatic event (Cugerone et al. 2021b; Fig. 1C). In the PAZ, many districts
151 are mostly composed of this type (i) sphalerite such as the Bentailou-Liat mine (Cugerone et
152 al. 2021b), Pierrefitte, and Cinco Villas districts which were mined during the 20th century
153 (Pouit 1986; Pesquera and Velasco 1989; Cugerone et al. 2018b, 2021b). At Bentailou-Liat,
154 Pb-Zn mineralization is hosted in Cambro-Ordovician marbles and located in the upper-flank
155 of a pluri-kilometer-scale recumbent F1 fold (García-Sansegundo and Alonso 1989; Cugerone
156 et al. 2018b, 2021b). Type (i) sphalerite is probably related to a skarn-like origin and has
157 endured regional low-grade M1 metamorphism (300-400 °C) with the occurrence of

158 muscovite associated with sphalerite (Cugerone et al. 2021b). Type (i) sphalerite exhibits
159 polygonal grain boundaries and is characterized by the absence of Cu, Ga and Ge in the
160 crystal lattice (Cugerone et al. 2021a).

161 Type (ii) sphalerite occurs in crosscutting Late-Variscan veins (Cugerone 2019;
162 Fig. 1C), probably genetically related to the remobilization of Variscan stratabound ore in
163 vertical Variscan S2 cleavage (Cugerone et al. 2018b). In the Pale Bidau-Argut-dessus
164 district, these meter-scale veins are hosted in Ordovician calc-schists and are mostly sub-
165 vertical and parallel to the N090°-to-110°E trending S2 Variscan cleavage (Cugerone et al.
166 2018b). One decimeter-scale crosscutting vein in the Liat deposit also shows a vertical
167 orientation, crosscutting earlier Variscan stratabound veins. Fluid inclusion analyses
168 demonstrate that the mineralizing fluid had a typical metamorphic fluid signature of medium
169 temperature (200-260 °C), low-salinity (<10 wt.% NaCl eq.) and low Cl/Br ratio (Johnson et
170 al. 1996; Cugerone 2019). However, secondary fluid inclusions with low-temperature (100-
171 150 °C) and medium salinity (10-15 wt.% NaCl eq.) are generally observed in fractures,
172 inferring the circulation of a secondary hydrothermal fluid superimposed on the pre-existing
173 Late-Variscan Pb-Zn mineralization. In the type (ii) sphalerite, millimeter-thick iron-rich
174 zones are spatially associated with a pronounced late structural cleavage mainly observed
175 with grain size variations (from 5 µm to pluri-millimeter size). Ge-oxides (up to 70 wt.% Ge)
176 are essentially reported in the finest sphalerite-recrystallized matrix or close to type (ii)
177 sphalerite twin boundaries (Cugerone et al. 2018a and Cugerone et al. 2021a). The
178 recrystallization age is still not clear between Late-Variscan and Pyrenean-Alpine
179 deformation times because of the lack of field evidence and suitable minerals associated with
180 deformation structures. Furthermore, the structural cleavage related to preferential
181 recrystallization planes in type (ii) sphalerite shows the same orientation as the Variscan S2
182 cleavage (N090-110°) in the host-rock, but Pyrenean-Alpine cleavage could have a similar

183 orientation so orientation is not diagnostic of age (Cochelin et al. 2017; Cugerone et al.
184 2018b).

185 Post-Variscan crosscutting veins are generally enriched in critical metals (especially
186 Ge, Ga). These veins are associated with the circulation of low-temperature (< 150 °C) and
187 medium-high-salinity hydrothermal fluid (> 15 wt. % NaCl eq.)(Munoz et al. 1994; Cugerone
188 2019).

189 Type (iii) sphalerite appears in crosscutting veins from the Saint-Salvy Zn–Ge–Ag(–
190 Pb–Cd) deposit, in the MN massif (Fig. 1C). This deposit is hosted in Cambrian black-schist
191 and structurally-controlled by the contact aureole of the Late-Variscan Sidobre granite
192 (Cassard et al. 1993; Munoz et al. 1994). The main metric-scale crosscutting veins
193 mineralization (named M4) was mined until the 1970s and consists of a cockade breccia
194 cemented by type (iii) sphalerite, siderite and quartz (Cassard et al. 1993; Munoz et al. 1994).
195 These veins are genetically related to the Lias-Dogger transition during an extensive strike-
196 slip regime. No significant post-mineralization deformation is documented at Saint-Salvy and
197 sphalerite exhibit euhedral crystals, with common primary chemical zoning (sector zones and
198 rhythmic bands; Johan 1988; Belissont et al. 2014).

199 Type (iv) sphalerite is observed in post-Variscan crosscutting veins from the PAZ, and
200 is generally hosted in folded Devonian cordierite-schist (Anglas), marble (Arre) and/or
201 Carboniferous magmatic rocks (Cierco; Reyx 1973; Johnson et al. 1996; Munoz et al. 2016;
202 Fig. 1C). The Arre-Anglas district was mined in the 20th century and is located at the western
203 part of the PAZ close to a Pyrenean-Alpine regional thrust (Eaux-Chaudes thrust; Cugerone et
204 al. 2018b). The Arre-Anglas vein system is post-Variscan in age, associated with the
205 circulation of low-temperature (< 150 °C) and high-salinity (> 15 wt.% NaCl. eq.) fluids
206 (Cugerone 2019). The Cierco vein system is hosted in the central part of the PAZ, south of the
207 Maladeta Variscan massif and shows similar low-temperature (< 150 °C) and high-salinity

208 (> 15 wt.% NaCl. eq.) fluids (Johnson et al. 1996). These veins have experienced low-grade
209 plastic deformation (< 300 °C) and have preserved dynamic recrystallization features
210 (Cugerone et al. 2020), which are interpreted as Pyrenean-Alpine in age (Cugerone et al.
211 2021b). Germanium-sulfides (up to 10-15 wt.% Ge) are observed in the recrystallized
212 domains or close to twin boundaries in coarse parent grains (Cugerone et al. 2021a).

213 **3. Methods**

214 The four studied types of sphalerite (i, ii, iii, iv) display heterogeneous grain sizes
215 (from 1-2 μm to few mm), colors (yellow to dark red) and trace elements distribution (sector
216 zones, rhythmic bands, millimeter-thick chemical zones). They show different deformation
217 imprints at macroscale, from weakly deformed with euhedral millimeter-scale crystals to
218 totally recrystallized and recovered with polygonal coarse grains. The studied sphalerite were
219 in-situ sampled, in underground galleries within the Bentaillou-Liat district (type i), or in
220 outcrop within the Pale Bidau (type ii) and Arre-Anglas (type iv) Pb-Zn districts (Fig. 1B).
221 The weakly-deformed sample (type iii) was collected in the Saint-Salvy Zn-Ge-Ag(-Pb-Cd)
222 deposit (Montagne Noire, Fig. 1B) from the main mineralized zone (M4 veins; Munoz et al.
223 1994).

224 Electron-Backscattered Diffraction (EBSD) maps were performed on fourteen
225 sphalerite thin sections (30 μm thick) with a Camscan Crystal Probe X500FE SEM-EBSD at
226 Géosciences Montpellier (CNRS – University of Montpellier, France). This technique
227 requires a well-polished surface and a last step of polishing at 0.25 μm using a Vibromet
228 polisher with 150 g of pressure on a polyurethane layer with colloidal silica, to maximize
229 EBSD band indexing on sphalerite. Condition of acquisition were a voltage of 20 keV and
230 probe current of 5 nA with a working distance of 25 mm under a 2 Pa low vacuum. The
231 samples surface was positioned horizontally at 20° to the incident electron beam to improve
232 the capture of the diffracted electrons. Energy dispersive spectrometry (EDS) maps were

233 simultaneously acquired during EBSD analyses. Sphalerite was systematically indexed as a
234 cubic mineral and match units used for sphalerite band indexing were derived from published
235 crystallographic data from Villars and Calvert (1991). The measurement steps were
236 methodically chosen below 5 μm , with up to 0.5 μm for the lowest value. Oxford Instruments
237 Aztec and Channel 5 softwares were used to generate EDS and EBSD maps. The equivalent
238 circle diameter method was used to calculate grain size, with a cutoff fixed at 2 pixels for the
239 smaller grains. Misorientation boundaries are the differences in crystallographic orientation
240 between two neighboring EBSD measurements (Randle et al. 2001), and are grouped,
241 between 2-5°, 5-10°, 10-15° for the low-angle boundaries, above 15° for the grain-boundary,
242 and 60° for the twin ($\Sigma 3$ about [111]) boundary. Short deviance of twin misorientations
243 between 58 and 62° is related to polishing artefact on the surface close to twin boundaries
244 rather than consistent changes in common cubic 60° twin misorientation. For each histogram
245 of the misorientation angle distribution plotting neighbor-pair (correlated) and random-pair
246 (uncorrelated) misorientations, a lower cutoff of 2° and a bin width of 2° was chosen. Grain
247 orientation spread (GOS; Brewer et al. 2010) and grain reference orientation deviation
248 (GROD; Rui et al. 2018) calculations were performed considering twins ($\Sigma 3$) as grain
249 boundaries to prevent misorientation artefact from 60° twins. Inversely from GOS calculation,
250 we did not include twins as grain boundaries for aspect ratio and long axis slope calculations
251 to prevent high aspect ratio and long axis slope artefacts, respectively. The error on each
252 crystal orientation measurement is generally between 0.3 and 0.5°.

253 Laser-induced breakdown spectroscopy (LIBS)-based mapping was performed at the
254 Institute Lumière Matière, University of Lyon 1 (France). This desktop system was used to
255 map the distribution of Ge, Cu, Ga in three samples from the type (ii) from Pale Bidau, the
256 type (iii) from Saint-Salvy, and type (iv) from Arre crosscutting veins deposits. No LIBS map
257 was acquired on type (i) sphalerite because of the low Cu, Ge, Ga and In contents reported by

258 Cugerone et al. (2021a). LIBS mapping is an all-optical analytical technique, allowing the
259 mapping of metallic elements in various type of minerals at a micrometer spatial resolution
260 with a sensitivity at the ppm level (Cáceres et al. 2017). During the analysis, the sample
261 surface is scanned ablating 2-3 μm of the sample, in a pixel-by-pixel manner to induce the
262 breakdown and sparks of the material. The light radiation emitted by the plasma is then
263 collected by an optical system and analyzed using a spectrometer. The samples were analyzed
264 using a Nd:YAG laser with a pulse energy of about 600 μJ operating at 100 analyses per
265 second (100 Hz), and a lateral resolution of 13 μm (i.e., distance between two consecutive
266 laser shots). The spectrometer was configured in the spectral range of 250-330 nm to detect
267 intense lines of Ge (265.1 nm), Cu (324.7 nm) and Ga (294.4 nm). On the two same samples
268 analyzed by LIBS-mapping, LA-ICP-MS measurements (Cugerone et al. 2021a) were
269 acquired to quantify LIBS measurements. Full LIBS maps are available in ESM1 (type ii),
270 ESM2 (type iv) and in Cugerone et al. (2021a) for type (iv).

271

4. Results

272 4. Petrographic and textural observations

273 In this study, four types of sphalerite textures are observed (Fig. 2) showing variable
274 recrystallization imprints: weakly deformed with euhedral millimeter-scale crystals (type iii),
275 totally recrystallized with polygonal coarse grains (type i), and partly recrystallized with
276 coarse-small grain texture (type ii and iv). These types are described below:

- 277 • Type (i) sphalerite is from a stratabound vein (Bentailou-Liat). It is mostly coarse
278 grained (up to few millimeter in size; 80 vol%) with polygonal shapes, or “foam”
279 texture and dark-reddish color in transmitted light, associated with minor calcite,
280 galena, pyrite and pyrrhotite (Fig. 2A-B).
- 281 • Type (ii) sphalerite is from crosscutting veins (Pale Bidau, Argut-dessus and Liat). It
282 is commonly hosted in low-grade calc-schist and sphalerite is the main mineral

283 component of these veins (~ 70 vol.%) with minor galena, pyrite, chalcopyrite and
284 Ge-minerals (mostly oxides), in a gangue of quartz and calcite (Figs. 2C and 2D). In
285 hand-specimen, sphalerite crystals are poorly visible due to the absence of grain-
286 related chemical zones. Only chemical light- to dark-brown millimeter-thick zones can
287 be identified. However, under an optical microscope, coarser grains can locally be
288 detected (up to millimeter size; Fig. 2D).

289 • Type (iii) sphalerite is from crosscutting veins (Saint-Salvy). It is essentially
290 composed of coarse millimeter euhedral crystals with no apparent recrystallization
291 texture (70 vol.%) in a gangue of siderite and quartz (Fig. 2E) around clasts of schist.
292 At micron-scale and with transmitted light, sphalerite shows various chemical zones
293 with occurrence of rhythmic bands and local dark-brown zones including sector zones,
294 generally following the typical shape of sphalerite {111} crystallographic faces (i.e.;
295 Johan 1988; Fig. 2E);

296 • Type (iv) sphalerite is from crosscutting veins (Arre-Anglas, Cierco). It exhibits
297 micrometer to coarse millimeter crystals (~ 70 vol.%) associated with minor galena
298 and Ge-minerals (sulfides) in a gangue of quartz. Sphalerite observed in transmitted
299 light is highly heterogeneous with occurrence of light to dark-brown color domains in
300 coarse millimeter crystals, which are mantled by a very fine-grained sub-vertical
301 matrix of light-brownish grains (Figs. 2F and 2H), certainly indicating a Pyrenean-
302 Alpine cleavage (i.e., Cretaceous; Cugerone 2019).

303 **5. Microstructural analyses of sphalerite**

304 **5.1.1. Quantitative textural analysis**

305 Sphalerite is a cubic mineral commonly found in a hextetrahedral habit with three
306 main crystallographic forms ({100}, {111} and {010}, Fig. 3A). In this study, no acicular or
307 wurtzite-like texture as previously shown by Pring et al. (2020), has been imaged by EBSD

308 method. In the four studied sphalerite types, EBSD maps evidence large grain size variations
309 (Fig. 3B). Between type (iii) euhedral-zoned and type (ii) and (iv) highly recrystallized
310 sphalerite, there is a significant grain size difference with a mean grain size of $375 \pm 527 \mu\text{m}$
311 and $15 \pm 19 \mu\text{m}$ (mean diameter with standard deviation), respectively. In type (iii) sphalerite,
312 a high proportion of $> 400 \mu\text{m}$ grains is observed with a small grain population ($n=76$;
313 Fig. 3B). In type (iv) sphalerite, ten grains reach a grain size above $400 \mu\text{m}$ but represent a very
314 small proportion compared to the total grain population ($n=25122$). Type (i) polygonal sphalerite
315 grains are generally coarser in size than type (ii) and (iv) recrystallized sphalerite with a mean
316 grain size of $84 \pm 211 \mu\text{m}$ (Fig. 3B).

317 Relationships between total sphalerite grain number per surface unit and grain
318 orientation spread (GOS) are shown in Figure 3C for the four studied sphalerite. The number
319 of grains per surface unit is a good indicator of the degree of recrystallization and the GOS is
320 a useful estimation of the intra-granular plastic deformation in a crystal (Hadadzadeh et al.
321 2018). Type (i) and type (iii) sphalerite show similar lower number of grains per surface and
322 low amounts of crystal plastic deformation although GOS values are sensibly higher in type
323 (i) sphalerite than in type (iii) sphalerite (threshold at $\sim 1.25^\circ$ and $\sim 0.5^\circ$, respectively;
324 Fig. 3C). For these type (i) and type (iii) sphalerite, the higher GOS values spread between 8
325 to 13° . In type (iv) sphalerite, higher number of grains per surface and GOS values are
326 observed, with a GOS threshold at 2.5° and higher values which may reach 17 to 30°
327 (Fig. 3C). In type (ii) sphalerite, number of grains per surface unit reaches the highest values
328 with up to $12\,000 \text{ grain/mm}^2$. GOS threshold for this texture is similar to type(i) sphalerite
329 with a GOS threshold at $\sim 1.25^\circ$ (Fig. 3C).

330 The calculated aspect ratio is equal to the ratio between the height and width of each
331 crystal and is a good evaluation of the two-dimensional crystal shape. Figure 3D compares
332 grain aspect ratios with the percentage of grains per surface unit. For all sphalerite grains,

333 aspect ratio values are essentially comprised between 1 and 3 with a maximum located at
334 ~ 1.5. Nevertheless, type (i) euhedral zoned sphalerite displays a higher aspect ratio, related
335 to the development of lamellar and more angular coarse grains.

336 **5.1.2. Microstructures in Variscan sphalerite vein**

337 • **Type (i) polygonal**

338 This sphalerite has a homogeneous coarse grained texture with frequent polygonal shape
339 (up to few millimeters; Fig. 4A). In Figure 4B, the uncorrelated misorientation angle
340 distribution is close to random (i.e. no overall CPO;). The correlated distribution is
341 nonrandom with a large peak (~0.2 relative frequency) for twins at 60° and a smaller peak
342 (about 0.35 relative frequency) at very low angles, consistent with subgrain development. In
343 four misorientation profiles from representative grains (Fig. 4C), very restricted number of
344 low-angle boundaries is confirmed, generally below 1° (< 15°; Fig. 4A and 4B). The rose
345 diagram of long axis slope does not show shape-preferred orientation (SPO; Fig. 4D). No
346 consistent lattice rotation is observed in pole figures of two representative grains (Fig. 4E).
347 Pole figures show a random/uniform crystallographic orientation despite a weak point
348 maximum of the (100) (maximum density = 2.61, Fig. 4E). Twin boundaries display a regular
349 straight and undeformed morphology, often regularly spaced with tabular aspect, and frequent
350 limited extension in grains. These twins are typically named “annealing-twins” (Gill 1969;
351 Guan et al. 2017, Fig. 4A).

352 • **Type (ii) polygonal and recrystallized**

353 This sphalerite type shows large grain-size heterogeneities, dividing the studied EBSD
354 area in three domains, vertically distributed (Figs. 5A and 5B): coarse, medium and fine-
355 grained zone.

356 The coarse grained zone is composed of coarse grains (>100 μm) with frequent curved
357 or lobate grain boundaries and rare small grains (<10 μm; Figs. 5B and 5D). Two

358 morphologies of twin boundaries (111) are observed: i) tabular twins, regularly spaced and
359 weakly-deformed, typical of “annealing-twins” (Mahajan et al. 1997); ii) deformed, curved
360 twins that thicken close to grain boundaries, characteristic of “deformation-twins” (Couderc et
361 al. 1985; Christian and Mahajan 1995; Figs. 5C, 5D and 6). Limited intra-granular plastic
362 deformation appears in the coarse grains, mostly at the interface with fine grained domain
363 (Figs. 5D and 5F) and are commonly expressed as vertically oriented 5° misorientation
364 lamellae (Fig. 5G), but intra-granular plastic deformation is still less present in the finest
365 fraction (Fig. 5C). Most of the sphalerite grain shapes are preferentially oriented vertically
366 (90° from the horizontal direction of the sample), parallel to the main cleavage (i.e., rose
367 diagram in Fig. 5E), but only a weak CPO (crystal preferred orientation) is observed on a pole
368 figure, on the (110) plane (maximum density = 3.47; Fig. 6). Pole figures of the coarse grain
369 labelled 1 and outlined in white in Fig. 6 display a rotation of the crystal lattice on (111)
370 and/or (110) directions with cumulative rotation of about $10\text{-}15^\circ$ (Fig. 5G and 6).

371 The fine-grained zone is essentially composed of small grains ($<25\ \mu\text{m}$) with anhedral
372 habit. Twin boundaries are much more represented than in coarse grained zone with
373 systematic simple or double twinning, with undeformed morphology and full extension in
374 each grain, typical of annealing-twins (see zoom on Fig. 5D). There are fewer low
375 misorientation boundaries (mostly $<5^\circ$) in these sphalerite grains compared to the coarse-
376 grained zone (Figs. 5C and 5D) and is confirmed with the $<10^\circ$ rotations observed on inverse
377 pole figure of four randomly selected small grains (Fig. 6). Pole figures show a near random
378 or uniform distribution with a slight point maximum on the (111) plane (maximum
379 density = 2.37; Fig. 6).

380 The medium grain zone is a mix between small and coarse-size grains. In this area,
381 coarse grains with lobate shapes contain low angle misorientation (essentially $<5^\circ$) with
382 frequent local straight 5° misorientation lamellae or with rounded shape close to grain

383 boundaries, similar in size with surrounded small grain fraction (Fig. 5B and 5C. Pole figures
384 display a weak CPO (maximum density = 1.54) with $\langle 100 \rangle$ axes that show an ill-defined
385 small circle girdle, supporting the common preferred direction observed at the center of the
386 (111) pole figure (Fig. 6).

387 **5.1.3. Microstructures in post-Variscan sphalerite vein**

388 • **Type (iii) euhedral**

389 This sphalerite is intensely chemically zoned and precise distinction of grain-twin
390 boundaries is challenging with common optical microscopic observations (Fig. 7A). EBSD
391 analysis shows that sphalerite crystals have generally a coarse grain size with an average at
392 $377 \pm 527 \mu\text{m}$ (up to 3.2 mm) and a minimal grain size at $25 \mu\text{m}$. Grain boundaries are often
393 straight or slightly curved with sub-angular habit. The dark-brown sector-zones described by
394 Belissont et al. (2014), are generally coarse with up to $\sim 500 \mu\text{m}$ extension, and frequent
395 elongated or triangular-trapezoidal shapes, similar to the $\{111\}$ sphalerite growth faces
396 (Fig. 3A), whereas light and dark-brown rhythmic parallel bands exhibit variable
397 thickness/spacing and crosscut sector zonings and twin boundaries (Fig. 7A). Two
398 morphologies of $\{111\}$ growth-twins are identified with misorientation angles of $60^\circ (\pm 1-2^\circ,$
399 related to EBSD precision): a) frequent twins with a strict straight and undeformed shape,
400 parallel direction and regular twin widths (Fig. 7B); b) less frequent twins with straight but
401 irregular orientations with numerous intersections between them (Fig. 7B). The length of the
402 two morphologies of growth-twins is variable, from a few μm to hundreds μm and generally
403 spread along the whole grain. Low-angle ($<15^\circ$) misorientations are not frequent (Fig. 7C)
404 and are mostly located close to grain boundary or to misoriented growth-twins (Figs. 7B and
405 7D) and associated with thin lamellae of $5-10^\circ$ misorientation (Figs. 7D and 7E). Thin dark-
406 brown zones are observed in transmitted light in these low-angle misorientations (Fig. 7A).
407 These observations are consistent with the low GOS values obtained (i.e., 12.6° ; Fig. 3C) and

408 the weakly dispersed value on the pole figures analysis of two representative sphalerite grains
409 (Fig. 8). In Figure 7A, a well-developed sector zoning shows no clear relationship between
410 low-angle boundaries and the dark zone (Fig. 7E). Pole figures show a weak CPO along the
411 (100) plane despite the observed significant crystallographic dispersion (Fig. 8).

412 • **Type (iv) euhedral and recrystallized**

413 In transmitted light, this sphalerite type shows large, gradational light- to dark-brown
414 domains crossed by late fractures (Fig. 9A). The main characteristic of this sphalerite-type is
415 the heterogeneity in grain size, evidenced by pluri-millimeter coarse crystals with frequent
416 lobate boundaries close to pluri-micrometer grains, mostly localized in 10-50 μm thick sub-
417 vertical cleavage and difficult to observe in transmitted light (150 μm thick; Fig. 9A and 9E).
418 At Anglas, type (iv) sphalerite grain contain twin-boundaries with deformed or bent
419 morphology and that thicken close to grain boundaries ($>15^\circ$) where a higher density of low-
420 angle boundaries ($<15^\circ$) appears (Fig. 9B). This is typical of “deformation-twins” (Fig. 9B
421 and 9H). Nonetheless, some small straight twins are frequently observed in the fine grain
422 cleavage domains but also locally, some deformed “growth-twins” in the coarse grains with
423 regular and no thicker extent close to grain boundary. Low angle misorientations ($<15^\circ$) are
424 frequent (Fig. 9C, 9G and 9I) and mainly located in the coarse grain fraction. Three profiles
425 perpendicular to deformation-twins show the presence of thin ($5\text{-}10^\circ$) lamellae, horizontal in
426 the sample and preferentially aligned in the continuation of deformation-twins (see green
427 profile and black arrows; Fig. 9J). Nonetheless, vertical or oblique $5\text{-}10^\circ$ lamellae are
428 observed in the two mapped areas. In the area-2, a large amount of misorientation is observed
429 in areas where no growth- and twin-deformation are detected (see white arrows, Fig. 9F).
430 Thin $5\text{-}10^\circ$ lamellae may appear in the continuation, or at 60° of deformation-twins (Fig. 9E).
431 Furthermore, in the coarse sphalerite grain of the area-2, a progressive misorientation increase
432 of about 30° is observed from the upper-central part to the lower external part (Fig. 9J).

433 Type (iv) sphalerite from Arre is composed of coarse infra-millimeter size grains
434 mantled in a small pluri- μm grain matrix. Coarse grains generally reach smaller sizes than in
435 Anglas (up to 1.6 mm and 3.6 mm, respectively) and contain a limited amount of twinning,
436 with generally growth-twinning much more represented than deformation-twins (Fig. 10A).
437 The main cleavage marked by the fine grain fraction frequently appears parallel to growth-
438 twin in fine-fraction grains. Furthermore, straight, and regular twinning typical of annealing-
439 twins are frequently observed in the fine grain matrix. Low-angle misorientation boundaries
440 ($< 15^\circ$) are abundant mainly in coarse grains but also represented in small grain fractions
441 (Figs. 10B and 10D). Misorientation boundaries below 4° are two times higher in frequency
442 than twin boundaries (Fig. 10D) and generally form thin lamellae in coarse grains, with
443 parallel or perpendicular directions to the main cleavage direction (Figs. 10C and 10E). In the
444 high-resolution EBSD map from type (iv) sphalerite (Arre; step of measurement: $0.5 \mu\text{m}$;
445 Fig. 11), twinning appears to limit the development of low angle misorientations in sphalerite.
446 In a coarse grain with abundant vertical growth-twins parallel to the main cleavage direction
447 (see Figs. 11A and 11B) a short area devoid of twin is identified with abundant low-angle
448 misorientations interpreted as lattice sliding/shearing during plastic deformation. At an angle
449 of $60\text{-}70^\circ$ from twin boundaries (Figs. 11A and 11C, close to dark-orange cumulative
450 misorientation profile), $< 5^\circ$ misorientation lamellae are observed and between these
451 structures and adjacent twin boundaries, local plumose-like structures are identified with
452 progressive misorientation from the intersection of twin-lamellae to the grain core (see black
453 arrow on the lower-right- part of Fig. 11B). Compared to sphalerite grains with abundant twin
454 boundaries and low-amounts of low-angle misorientations, grain without twin contain
455 extensive low-angle misorientations and subgrains (Figs. 11D and 11E). In these sphalerite
456 grains, progressive lattice deformation is expressed by thin and short perpendicular $< 5^\circ$
457 lamella, and up to 25° cumulative misorientation detectable on the pole figure (Fig. 12). This

458 ductile deformation is located more in the grain rim than in the grain core (Figs. 11E, 11F and
459 12). The small grain fraction ($< 100 \mu\text{m}$) with annealing-twins also contains significant low-
460 angle cumulative misorientation with up 10 to 15 °C (Fig. 12). There is no bulk CPO in small
461 or coarse grain fractions.

462 **6. Chemical composition of sphalerite**

463 **6.1.1. Type (ii) sphalerite**

464 A large type (ii) sphalerite area (16 x 2.5 mm) from Pale Bidau observed in
465 transmitted and reflected light (Figs. 13A and 13B) has been analysed with EBSD (see the
466 two grain-size maps in Fig. 13B). The distribution of Cu, Ga, and Ge contents is measured
467 with LIBS mapping (and quantified with four LA-ICP-MS spots from Cugerone et al. 2021a)
468 and an element abundance profile is proposed to understand the correlation between these
469 elements (Fig. 13C-F). The Cu, Ga, Ge contents are highly heterogeneous and define
470 millimeter-to-centimeter thick chemical zones, that are parallel to the tectonic cleavage. These
471 zones are unrelated to Fe-content defined by sphalerite color bands (Fig. 13A), but to
472 sphalerite grain size (Fig. 13B). Coarse grain domains ($> 100 \mu\text{m}$; Fig. 13) are depleted in Cu,
473 Ga and Ge with content below 50 ppm. In these domains, local Cu contents are concentrated
474 at sphalerite grain boundaries (Fig. 13C) and not in the sphalerite crystallographic lattice. In
475 the fine-grained fraction ($< 100 \mu\text{m}$), domains with >100 ppm of Cu and Ga appear relatively
476 homogeneous at microscale on the map. But the presence of nano to micro inclusions rich in
477 Cu-Ga-Ge is inferred, based on the numerous spikes observed on the profile (Fig. 13B), and
478 on the frequent occurrence of Cu and Ge-minerals (see cyan and yellow colors, respectively;
479 Fig. 13C-E). At microscale, Ge-minerals are mostly composed of carboirite
480 ($\text{GeFeAl}_2\text{O}_5(\text{OH})_2$) and brunogeierite (GeFe_2O_4), and locally, Cu-minerals occur as
481 micrometer scale chalcopyrite grains.

482 **6.1.2. Type (iii) sphalerite**

483 In type (iii) sphalerite from the Saint-Salvy deposit, EBSD and LIBS maps are shown
484 in Figure 14, in the same area as Figure 7. Based on Bélistont et al. (2014), Bélistont et al.
485 (2016) and Fougrouse et al. (2023), type (iii) sphalerite shows two types of trace element
486 zoning. A first type is composed of angular and straight rhythmic bands from dark brown to
487 light yellow colors, not restricted to a particular sphalerite crystal (Figs. 14A and 14B). The
488 dark rhythmic bands are relatively enriched in Fe, Cd, Cu, Sn and In, with low contents in Ga
489 and Ge (142 ± 96 ppm Ge; LA-ICP-MS data from Bélistont et al. 2014). Rhythmic bands
490 rich in Sn and In are rare in the sample analysed (Fig. 14H), but are generally more developed
491 in the earlier stage of sphalerite precipitation (see arrows representing growth direction,
492 Fig. 14B; ESM1). Irregular dark brown zones, including sector zonings, constitute a second
493 type of zoning, which appear late in crystal growth history compared to rhythmic bands (see
494 zoom in Fig. 14B), and shows higher enrichments in Ge, Cu, Ga, Sb, Ag (Figure 14 and
495 ESM 1; mean of 1102 ± 716 ppm Ge; LA-ICP-MS data from Bélistont et al. 2014).
496 Combining EBSD and LIBS maps, similar dark brown zones are also visible along grain
497 boundaries, in twin boundaries and in low angle misorientation boundaries ($< 15^\circ$; see the
498 circled areas Figure 14). On the LIBS map, the Cu and Ge do mimic the triangular sector
499 shapes (Bélistont et al. 2014), but they also have linear shapes often close or along sector
500 zones (see circle 4 in Figs. 14C and 14D).

501 **6.1.3. Type (iv) sphalerite**

502 In type (iv) sphalerite from the Arre deposit, EBSD and LIBS maps are shown in
503 Figure 15, in the same area as Figure 10. Only Ge and Cu contents are shown because Ga
504 contents were below detection limits in these grains (< 15 ppm Ga).

505 As shown by Cugerone et al. (2019), dark-brown domains with Cu-Ge rich contents
506 (up to few hundreds of ppm) are only located in the coarse sphalerite grains whereas light

507 domains, depleted in Ge and Cu may be located in coarse and small recrystallized grain
508 fraction. In Figure 15, light domains in coarse grains depleted in Cu-Ge are systematically
509 associated with a large amount of low-angle misorientation boundaries (2-15°). Dark Cu-Ge-
510 rich domains are mainly detected in areas lacking low-angle misorientation boundaries
511 (Fig. 15). At microscale, the highest contents in Ge are represented by Ge-minerals (briartite
512 $(\text{GeCu}_2(\text{Fe}, \text{Zn})\text{S}_4)$) and are mostly located close to twin or low-angle misorientation
513 boundaries (see yellow dots; Fig. 15B and 10A). In Fig. 15D, a cumulative misorientation
514 profile is compared to Ge and Cu contents from LIBS maps. Higher Ge and Cu contents
515 hosted in microscale Ge-minerals are reported close to 10-15° lamellae. However, relative
516 high Ge-Cu contents (100-300 ppm Ge; 400-500 ppm Cu) are also reported in areas with low
517 2-15° misorientation (see low dislocation areas in Fig. 15D).

518 **5. Discussion**

519 **6.1.4. Relationship between microstructures and ore genesis**

520 In the Variscan basement of the Pyrenean Axial Zone (PAZ) and Montagne Noire
521 (MN), EBSD microstructural observations coupled to microchemistry on various sphalerite
522 mineralization integrated in a regional scale model provide insightful evidence on the timing
523 relationships between Pb-Zn veins (Fig. 16).

524 In the MN and PAZ massifs, Pb-Zn veins formed in two stages during Variscan and
525 post-Variscan tectonics (Cugerone et al. 2021a). Similarly, this study shows two distinct
526 groups of Variscan and post-Variscan sphalerite veins composed of type (i)-(ii) polygonal
527 crystals and type (iii)-(iv) euhedral crystals, respectively. Polygonal or “annealed” type (i)
528 sphalerite with no chemical zones in Cu, Ga and Ge is typical of Variscan and
529 metamorphosed sphalerite (Figs. 2 and 4) and is similar to textures observed in Liat,
530 Pierrefitte (Cugerone 2019; Cugerone et al. 2023) and in the Cinco Villas massif (Pesquera

531 and Velasco 1993). Type (ii) sphalerite from Pale Bidau shows millimeter-thick shear-bands
532 composed of very fine recrystallized grains ($< 50 \mu\text{m}$). These shear bands are hosted in a
533 previously coarse polygonal sphalerite similar to type (i) sphalerite ($> 100 \mu\text{m}$; Fig. 3C) and
534 are associated with abundant annealing-twins (Figs. 5D and 6). The origin of type (ii)
535 sphalerite veins could be related to remobilization of nearby Variscan stratabound bodies in
536 pre-existing Variscan S2 cleavage (Cugerone 2019).

537 Based on their close structural, textural and chemical characteristics, the origin of type
538 (iv) sphalerite is similar to the weakly deformed type (iii) sphalerite. The main difference
539 between type (iii) and type (iv) sphalerite is the superimposition of Pyrenean-Alpine thrusting,
540 involving significant textural and chemical modifications to type (iv) veins. The type (iv)
541 sphalerite from Arre-Anglas is partly dynamically recrystallized with Cu-Ga-Ge enrichment
542 preferentially located in dark-brown chemical zones and/or in micrometer Ge(-Cu) minerals
543 (briartite; Fig. 15). The development of fine grained sphalerite in domains parallel to the
544 regional tectonic cleavage is interpreted as deformation and dynamic recrystallization,
545 certainly associated with percolation of hydrothermal low-temperature fluid and metal
546 redistribution ($< 150 \text{ }^\circ\text{C}$; (Cugerone 2019; Cugerone et al. 2021a). Many intragranular
547 dislocations are often located in thin lamella within large grains, and could evidence
548 prolonged response of the large grains to deformation and/or multiphase deformation and
549 recrystallization events (Figs. 9, 10 and 11).

550 **6.1.5. Deformation mechanisms of sphalerite**

551 A few studies have focused on the deformation mechanisms of sphalerite, either in
552 natural or experimental systems (Kelly and Clark 1975; Siemes and Borges 1979; Kollenberg
553 and Siemes 1983; Couderc et al. 1985; Cugerone et al. 2020; Paradis et al. 2023).
554 Understanding sphalerite deformation mechanisms is of major importance to unravel the

555 processes and metamorphic conditions that produce deformed and recrystallized textures, but
556 also to constrain the potential for lattice distortion to affect trace metal enrichment.

557 In this study, four sphalerite textures have been described based on their grain size
558 distribution, grain-twin boundaries, and crystal plastic deformation style. In type (i) sphalerite,
559 polygonal grains show low amount of intragranular dislocation and straight and tabular
560 annealing-twins. All primary textural features have been fully erased during static
561 recrystallization and annealing, following low-grade metamorphism (300-450 °C). No
562 significant superimposed Pyrenean-Alpine recrystallization is found in type (i) sphalerite
563 probably because of the initial horizontal geometry of these stratabound bodies which
564 prevented sub-vertical deformation (stratabound bodies sub-parallel to the main compression).
565 Conversely, deformation and shear-bands are observed in the nearby Late-Variscan sub-
566 vertical veins from type (ii) sphalerite (Pale Bidau). Type (i) and (iii) sphalerite shares some
567 similarities (see Fig. 3) but the occurrence of tabular annealing-twins and absence of intra-
568 granular plastic deformation in type (i) sphalerite point to a different origins and mechanisms
569 of formation. Sphalerite is “softer” than pyrite (Stanton and Gorman 1968; Clark and Kelly
570 1973b; Siemes and Borges 1979). In the locality where type (iii) sphalerite has been collected,
571 no major deformational event is reported after sphalerite vein emplacement (Munoz et al.
572 1994; Bélistont et al. 2014). However, low angle misorientation boundaries close to grain or
573 twin boundaries appears in type (iii) sphalerite (Figs. 7 and 8). We infer that sphalerite can
574 develop subgrains and twins even at low strains and relatively low grade conditions.

575 In type (ii) and (iv) sphalerite, which were deformed at low temperature (< 300 °C),
576 numerous low angle subgrain boundaries (< 5°) are, in untwined crystals, numerically more
577 abundant close to the edge of grains (Figs. 11D and 12). Furthermore, the evidence of
578 porphyroclastic coarse grains mantled by small, recrystallized daughter crystals suggests
579 plastic deformationumulative within-grain lattice rotations are observed and can progressively

580 reach up to 20-30° in a single grain (Figs. 11E and 11F). These subgrain boundaries or
581 dislocation walls are often organized in deformation lamellae and bands, supporting their
582 formation by dislocation creep mechanisms (Cox 1987; Hirth and Tullis 1992; Barrie et al.
583 2007). Daughter-recrystallized sphalerite generally contains a small amount of low-angle
584 misorientation (Figs. 5C, 5D and 10B) compared to the parent porphyroclast grains, especially
585 in the type (ii) sphalerite, which suggests the operation of a subgrain rotation (SGR)
586 recrystallization regime during recovery (Drury and Urai 1990; Hirth and Tullis 1992).

587 However, in sphalerite, some differences with the conventional SGR regime exist. In
588 the type (ii) sphalerite, the plastic deformation and dynamic recrystallization are primarily
589 located in millimeter-scale shear-bands (fine grained zones; Fig. 5) compared to type (iv)
590 sphalerite

591 If we consider similar paleo-stress in type (ii) and (iv) sphalerite, primary sphalerite
592 texture and chemistry seems to have played a key role in the localization of deformation.
593 Type (i) to (ii) sphalerite are composed of chemically homogeneous sphalerite (Cugerone et
594 al. 2021a). Polygonal starting grains respond to palaeo-stress in type (ii) by recrystallization
595 along millimeter-scale shear-bands (fine grained zones; Fig. 5) of the recrystallized areas (Fig.
596 2C-D and 5), parallel to S2 cleavage observed in the host-rock. Type (iii) to type (iv) are
597 composed of chemically heterogeneous sphalerite with significant variations in chemical
598 impurities (Cu, Ge, Ga; Fig. 15 and 16; Fougereuse et al. 2023). Euhedral starting grains
599 respond to paleo-stress in type (iv) by recrystallization along variably oriented recrystallized
600 bands (~100-500 µm width; Figs. 10 and 11). The primary chemical heterogeneity was
601 certainly an additional factor influencing the orientation of recrystallized band in type (iv)
602 (Fig. 2H). These chemical impurities may cause distortion as these cations are of different
603 size than Zn, causing instabilities in the sphalerite structure, and triggering the formation of

604 inherent planes of weakness where deformation and recrystallization may be preferentially
605 located.

606 Another major difference with the common SGR model is the frequent occurrence of
607 twin boundaries in sphalerite inherited from primary processes, such as growth-twins (Šrot et
608 al. 2003), or metamorphic processes such as deformation-twins (Fleet 1983) and annealing-
609 twins (Lawrence 1973). Twin boundaries may have a key impact on the deformation
610 localization within sphalerite. For example, a high number of growth-twins can significantly
611 prevent intragranular deformation in the entire crystal and therefore, may cause hardening of
612 sphalerite lattice (Burkhard 1993; McCarley and Tin 2019). Twins frequently influence
613 deformation and recrystallization distribution as described for a large number of
614 minerals/materials (Cox and Etheridge 1984; Burkhard 1993; Bestmann and Prior 2003; Guan
615 et al. 2017). Compare to primary growth-twins, deformation-twins are created to
616 accommodate the onset of plastic deformation in sphalerite porphyroclasts, with glide
617 mechanisms, observed in type (iv) sphalerite from Anglas (Fig. 9; Cox and Etheridge 1984;
618 Guan et al. 2017). When deformation increases, strain/dislocation may be accommodated by
619 twins, which may restrict the number of dislocations in the lattice (Fig. 9F). But in areas with
620 higher plastic deformation, the first subgrain boundaries nucleate in or close to the main
621 crystallographic heterogeneities such as grain boundaries, growth, or deformation-twin
622 boundaries, (Figs. 9B and 10A), as evidenced by frequent low-angle misorientation
623 boundaries ($< 15^\circ$) and recrystallized crystals in or close to isolated growth and deformation-
624 twins (Fig. 11).

625 In dynamically recrystallized domains (type ii and iv), despite a shape preferred
626 orientation only observed in type (ii), no consistent CPO is observed in sphalerite, which
627 could testify for the occurrence of grain boundary sliding during dynamic recrystallization
628 (Barrie et al. 2007). Lack of CPO related to deformation may be related to the widespread

629 development of annealed-twinned crystals with random orientation. A more probable
630 hypothesis explaining the absence of CPO is the presence of a large number of slip systems
631 (12) on {111} reported by Siemes et al. (1973; 1979) and Couderc et al. (1985), which are
632 detected in our samples with frequent rotation on (111) (Figs. 6 and 8).

633 **6.1.6. Chemi al zoning in sphalerite**

634 In weakly deformed type (iii) sphalerite, combining EBSD and LIBS maps highlights two
635 main textures hosting Cu, Ga, Ge (Fig. 14) that are more complex than what has been
636 mentioned in Bélistont et al. (2014). Early straight light to dark brown rhythmic bands
637 parallel to growing crystal faces are mostly enriched in Fe, Cd, Sn and In (mean of
638 2.5 ± 0.3 wt.%, 3535 ± 815 , 876 ± 534 , and 234 ± 238 ppm, respectively), but with relative
639 low contents of Cu, Ga and Ge (mean of 2447 ± 1014 , 332 ± 201 , and 142 ± 96 ppm Ge,
640 respectively). Based on the microscale distribution being only in the rhythmic bands, these
641 elements are probably incorporated in the sphalerite crystal lattice during primary growth. The
642 nanoscale study of Fougrouse et al. (2023) did not provide any measurement on rhythmic
643 bands in sphalerite. Late dark brown zones including sector zones (see circle 1 in Figs. 14A
644 and 14B), late dark-brown elongated structures along grain boundaries or in growing crystal
645 faces (see circles 2, 3 and 4 in Figs. 14A and 14B), are superimposed on rhythmic bands, with
646 higher enrichments in Cu, Ga, Ge, Ag (mean of 4003 ± 1713 , 359 ± 264 , 1102 ± 716 ,
647 354 ± 230). However, the occurrence of these dark brown zones is not only controlled by
648 crystal faces (such as {111} faces with triangular shape; Bélistont et al. 2014) but also by
649 growing crystal edges, grain boundaries, low angle misorientation ($< 15^\circ$), twin boundaries
650 (Fig. 14). Based on these observations, we infer that the dark brown zones and related Cu-Ga-
651 Ge incorporation are late compared to the formation of rhythmic bands. Elongated dark brown
652 zones (see circle 4 in Figs. 14A and 14B in growing crystal edges may be synchronous to
653 sector zones.

654 Based on the nanoscale study of Fougrouse et al. (2023), in the dark brown zones (sector
655 zoning and crystal edge traces), all the detected elements appear to be hosted in the sphalerite
656 lattice and entered in the sphalerite lattice by a substitution with Zn (Bélissont et al. 2016;
657 Bauer et al. 2019). As proposed by George et al. 2016, the difference in ionic radius between
658 Zn^{2+} and potential substituting cations could explain the zoning between element in early
659 rhythmic bands and late dark-brown zones. In the sphalerite lattice, Fe^{2+} , Cd^{2+} , In^{3+} and Sn^{3+}
660 show similar chemical zoning in rhythmic bands and they share very similar ionic radius
661 compared to Zn^{2+} (difference <15% in ionic radius; based on Shannon 1976). This similarity
662 could facilitate the incorporation of these elements in early rhythmic bands if their
663 concentration in the fluid is sufficient. But Ga^{3+} , Ge^{4+} , Sb^{3+} and Ag^+ are mainly concentrated
664 in late dark brown zones. All the various types of dark-brown zones such as sector zones,
665 growing crystal edges and grain/twin boundaries have similar content in Ga, Ge, Sb and Ag,
666 despite having internal variations in these elements and different size (sector zones are
667 typically larger, 50-250 μm ; Fig. 14). Gallium, Ge, Sb, Ag show differences of 21, 36, 26 and
668 73% with Zn^{2+} ionic radius, respectively (based on Shannon 1976). Then, dark brown zones
669 contain more cations with less similar ionic radius with Zn such as Ga^{3+} , Ge^{4+} , Sb^{3+} and Ag^+ .
670 However, Cu content is high in rhythmic bands and very high in dark brown zones (i.e.,
671 2447 ± 1014 and 4003 ± 1713 , respectively; Bélissont et al. 2014) but the Cu ionic radius is
672 identical to Zn (Shanon et al. 1976). Incorporation of Cu in the sphalerite lattice is generally
673 coupled with Ga, Ge, Sb Ag (Cook et al. 2009; Bélissont et al. 2016) and in the presence of
674 these cations in the fluid, Cu contents in sphalerite will increase, if the fluid composition is
675 sufficiently rich in Cu.

676 In deformed sphalerite, we report two mechanism of Cu-Ga-Ge redistribution (Fig. 16).
677 The first one is observed in type (iv) sphalerite, which highly depends on sphalerite grain
678 texture and the presence of low-angle misorientation boundaries (<15°; Fig 15). Germanium

679 and Cu are positively correlated (Cugerone et al. 2021a; Fougrouse et al. 2023). At
680 microscale in dark domains of type (iv) sphalerite, Cu contents are locally high (cyan dots;
681 Fig. 15), which support the presence of Cu-Ge minerals (like briartite) even in dark sphalerite
682 domains as mentioned by the nanoscale study of Fougrouse et al. (2023). In Figure 15D,
683 microscale briartite are noticed close to 10-15° lamellae in dark domains, observed nearby
684 Cu-Ge-poor light domains. Several studies show that the presence of intragranular
685 dislocations may act as a pipe or a trap for trace elements associated or not with a fluid
686 circulating in the plastically deformed mineral lattice (Vukmanovic et al. 2014; Piazzolo et al.
687 2016; Reddy et al. 2016; Fougrouse et al. 2019). Formation of large numbers of lattice
688 defects may increase the permeability and allow a low-temperature fluid to migrate and
689 remobilize pre-existing impurities (Piazzolo et al. 2016). In this model, before trace element
690 remobilization, light domains could have been dark and rich in trace elements such as Ge and
691 Cu. However, an alternative hypothesis consider a starting material before deformation
692 composed of dark and light domains (similar to type iii) and suggests a difference in their
693 plastic deformation response. The presence of trace element-rich nanoparticles in dark
694 domains may harden the sphalerite during crystal-plastic deformation (Fougrouse et al.
695 2023). In this study, we support the hypothesis of Fougrouse et al. 2023. During low-grade
696 metamorphic conditions (< 300°C), Ge and Cu could likely have exsolved into nanoscale
697 minerals. But based on Fig. 15D where higher Cu-Ge contents appears nearby deformation
698 10-15° lamellae, we suggest that lattice distortion and deformation structures located in the
699 dark domains may have locally facilitate diffusion of Ge and Cu.

700 In type (ii) sphalerite (Fig. 13), a second type of Cu-Ga-Ge redistribution is observed,
701 which is highly linked to pre-existing deformation structures such as grain size and shear
702 bands. Elevated contents in Cu, Ge and Ga are only observed in sub-vertical fine-grained
703 zones interpreted as shear-bands, hosted in polygonal sphalerite. Locally, Cu concentrations

704 (few tens of ppm Cu) are detected along coarse polygonal sphalerite grain boundaries. These
705 observations suggest a relative enrichment of Cu, Ga, Ge in the finer grained domains
706 (Fig. 13), which is here interpreted as resulting from late dynamic recrystallization and the
707 infiltration of a secondary Cu-Ge-Ga rich fluid preferentially in the more permeable active
708 sphalerite shear-bands (medium and fine-grained; Fig. 13). We suggest that circulation of a
709 Cu-Ga-Ge rich mineralized fluid may have percolated in various sub-vertical discontinuities
710 in the PAZ, especially in pre-existing sphalerite bodies such as Variscan polygonal sphalerite
711 (type i and ii). The pre-existing polygonal sphalerite in type (ii) sphalerite is considered to be
712 (Late)-Variscan in age (based on petrographic data), and may have represented preferential
713 pathways due to the widespread sub-vertical dynamic recrystallization features and the
714 enhanced porosity. Progressive variation in Cu-Ga concentrations in the shear-bands (Fig. 13)
715 are highly correlated to sphalerite grain size, and was probably mainly achieved by diffusion
716 processes assisted by a low-temperature fluid (<150 °C, Cugerone 2019). Nevertheless,
717 spatial distribution of Cu, Ge, and Ga contents differ (Fig. 13). Gallium is mainly
718 concentrated in millimeter-thick chemical domains, Ge is only detected in microscale Ge-
719 minerals (carboirite, brunogeierite) and Cu is observed both in millimeter-thick chemical
720 domains and micrometric chalcopyrite grains. Germanium did not significantly diffuse in
721 sphalerite, inducing low compatibility of Ge with sphalerite in these conditions. No nanoscale
722 study was performed on type (ii) sphalerite to assess if Cu and Ga are substituted into
723 sphalerite lattice or present as nano-inclusions so it cannot be excluded that their
724 incorporation occurs in sphalerite lattice and/or in nanoscale Cu and/or Ga-rich phases
725 (Fougerouse et al. 2023). But the element abundance profile in Figure 13C show spiked
726 variations in Cu and Ga contents, which could indicate the presence of Cu and Ga rich
727 nanoscale minerals. Nonetheless, Cu and Ga show a different microscale spatial distribution
728 compared to Ge with diffuse millimeter-thick Ga-Cu-rich domains (see rulers at ~7 and

729 13 mm; Figs. 13D and 13F) correlated to areas where Ge is punctually enriched. This
730 difference is interpreted to be associated with the size of inclusions, with larger size for Cu
731 and/or Ga-rich inclusions compared to Ge-rich inclusions.

732 In summary, in the Southern French Variscan terrane, vertically oriented stratabound
733 sphalerite veins similar to type (ii) sphalerite from Pale Bidau that were impacted by late-
734 Pyrenean deformation are potential targets for hosting similar Ge-minerals (Fig. 16).
735 Furthermore, the circulation of a secondary Cu-Ga-Ge rich fluid under probable low
736 temperature conditions (< 150 °C), preferentially in permeable actively deformed porosity and
737 sub-vertical structures, could explain the local occurrence of Ge-minerals in large stratabound
738 bodies reported by Laforet et al. (1981) and Oudin et al. (1988) in Bentaillou and Pierrefitte.

739 **6.Implications and conclusions**

740 Detailed microstructural analyses (EBSD) coupled to chemical imaging
741 (LIBS mapping) have been applied to four sphalerite-types occurring in a similar geological
742 setting (types i, ii, iii, iv). In Variscan veins, type (i) sphalerite is metamorphosed at low-grade
743 (< 300°C) and exhibit polygonal grains without intragranular dislocation and straight and
744 tabular annealing-twins. All primary textural features have been fully erased during static
745 recrystallization and annealing. In Mesozoic-Alpine veins, type (iii) euhedral sphalerite from
746 Saint-Salvy shows late Cu-Ge-Ga enrichment mainly observed in dark brown zones, located
747 in sector zonings, growing crystal edges, grain boundaries, low angle misorientation or twin
748 boundaries. In Variscan and Mesozoic-Alpine veins, type (ii) and type (iv) sphalerite have
749 been dynamically recrystallized, probably during the Cenozoic Pyrenean-Alpine deformation
750 event. During this tectonic event, two mechanisms of critical metal incorporation involving a
751 single Cu-Ge-Ga rich fluid are proposed (Fig. 16): (a) an in-situ exsolution of Cu-Ga-Ge
752 contents from a pre-existing Cu-Ga-Ge-rich sphalerite lattice to form mineral inclusions (b)
753 the circulation of a Cu-Ga-Ge rich hydrothermal fluid in surrounding rocks and precipitation

754 of secondary Cu-Ga-Ge-rich inclusions in shear bands hosted in pre-existing Cu-Ga-Ge-poor
755 sphalerite bodies. Based on numerous occurrences of Pb-Zn(-Ge) crosscutting veins in the
756 Pyrenean Axial Zone and the Massif Central (Fig. 1), this Cu-Ga-Ge-rich fluid appears to
757 have circulated on a regional scale in the upper-crust of the South of France Variscan terrane
758 during post-Variscan time, probably associated with the Pyrenean-Alpine orogeny. At
759 regional scale, it also shows that structural and chemical traps such as stratabound (vertical
760 and horizontal) sphalerite veins, impacted by late Pyrenean deformation, may generally host
761 Ge-minerals in the Pyrenees. At global scale, this study shows the key necessity of combining
762 EBSD and trace element mapping on deformed and undeformed sphalerite. Intragranular
763 plastic deformation and recrystallization features occur at low grade in sphalerite (< 300°C)
764 and are very difficult to observe with classical optical tools. Using EBSD coupled to LIBS
765 mapping on sphalerite can bring new information on vein origin and critical metals
766 concentration, even in apparent undeformed mineralized systems.

767

768

Acknowledgment

769 This study was funded through the French national program “Référentiel Géologique
770 de France” (RGF-Pyrénées) of the French Geological Survey (Bureau de Recherches
771 Géologiques et Minières; BRGM), and through the INSU-CNRS Tellus CESSUR program.
772 Bénédicte Cenki acknowledges funding from the European Union’s Horizon 2020 research
773 and innovation program under grant agreement No 793978. Alan Boyle is gratefully thanked
774 for his constructive comments on a preliminary version of the manuscript and an insightful
775 review. The authors also thank Christopher Beckett-Brown, Nicolas Mondillo and two
776 anonymous reviewers for their detailed and constructive reviews of the manuscript, Sarah
777 Brownlee and Hongwu Xu, for the careful editorial handling. The authors gratefully
778 acknowledge Christophe Nevado and Doriane Delmas for the exceptional thin section
779 preparation. Alexandre Cugerone thanks Denis Fougerouse for the fruitful discussion on the
780 general aspects of this paper.

781

782

References

- 783 Barrie CD, Boyle AP, Prior DJ (2007) An analysis of the microstructures developed in
784 experimentally deformed polycrystalline pyrite and minor sulphide phases using electron
785 backscatter diffraction. *J Struct Geol* 29:1494–1511. doi: 10.1016/j.jsg.2007.05.005
- 786 Bauer ME, Burisch M, Ostendorf J, Krause J, Frenzel M, Seifert T, Gutzmer J (2019) Trace
787 element geochemistry of sphalerite in contrasting hydrothermal fluid systems of the
788 Freiberg district, Germany: insights from LA-ICP-MS analysis, near-infrared light
789 microthermometry of sphalerite-hosted fluid inclusions, and sulfur isotope geochemi.
790 *Miner Depos* 54:237–262. doi: doi: 10.1007/s00126-018-0850-0
- 791 Bauer ME, Seifert T, Burisch M, Krause J, Richter N, Gutzmer J (2017) Indium-bearing
792 sulfides from the Hämmerlein skarn deposit, Erzgebirge, Germany: evidence for late-
793 stage diffusion of indium into sphalerite. *Miner Depos* 1–18. doi: 10.1007/s00126-017-
794 0773-1
- 795 Bélistont R, Boiron M-C, Luais B, Cathelineau M (2014) LA-ICP-MS analyses of minor and
796 trace elements and bulk Ge isotopes in zoned Ge-rich sphalerites from the Noailhac -
797 Saint-Salvy deposit (France): Insights into incorporation mechanisms and ore deposition
798 processes. *Geochim Cosmochim Acta* 126:518–540. doi: 10.1016/j.gca.2013.10.052
- 799 Bélistont R, Munoz M, Boiron M-C, Luais B, Mathon O (2016) Distribution and oxidation
800 state of Ge, Cu and Fe in sphalerite by μ -XRF and K-edge μ -XANES: Insights into Ge
801 incorporation, partitioning and isotopic fractionation. *Geochim Cosmochim Acta*
802 177:298–314. doi: 10.1016/j.gca.2016.01.001
- 803 Bestmann M, Prior DJ (2003) Intragranular dynamic recrystallization in naturally deformed
804 calcite marble: Diffusion accommodated grain boundary sliding as a result of subgrain
805 rotation recrystallization. *J Struct Geol* 25:1597–1613. doi: 10.1016/S0191-
806 8141(03)00006-3

- 807 Bons PD, Fusswinkel T, Gomez-Rivas E, Markl G, Wagner T, Walter B (2014) Fluid mixing
808 from below in unconformity-related hydrothermal ore deposits. *Geology* 42:1035–1038.
809 doi: 10.1130/G35708.1
- 810 Brewer LN, Field DP, Merriman CC (2010) Mapping and Measuring Plastic Deformation
811 Using EBSD. *B Electron Backscatter Diffr Mater Sci* 1–29. doi: 10.1007/978-0-387-
812 88136-2_18
- 813 Burkhard M (1993) Calcite twins, their geometry, appearance and significance as stress-strain
814 markers and indicators of tectonic regime: a review. *J Struct Geol* 15:351–368. doi:
815 10.1016/0191-8141(93)90132-T
- 816 Cáceres JO, Pelascini F, Motto-Ros V, Moncayo S, Trichard F, Panczer G, Marín-Roldán A,
817 Cruz JA, Coronado I, Martín-Chivelet J (2017) Megapixel multi-elemental imaging by
818 Laser-Induced Breakdown Spectroscopy, a technology with considerable potential for
819 paleoclimate studies. *Sci Rep* 7:1–11. doi: 10.1038/s41598-017-05437-3
- 820 Cassard D, Chabod JC, Marcoux E, Bourguine B, Castaing C, Gros Y, Kosakevitch A, Moisy
821 M, Viallefond L (1993) Mise en place et origine des minéralisations du gisement filonien
822 de Noailhac - Saint-Salvy Zn, Ge, Ag, (Pb, Cd) Tarn - France. BRGM BRGM R-376:82
- 823 Cathelineau M, Boiron MC, Fourcade S, Ruffet G, Clauer N, Belcourt O, Coulibaly Y, Banks
824 DA, Guillocheau F (2012) A major Late Jurassic fluid event at the basin/basement
825 unconformity in western France: $^{40}\text{Ar}/^{39}\text{Ar}$ and K-Ar dating, fluid chemistry, and
826 related geodynamic context. *Chem Geol* 322–323:99–120. doi:
827 10.1016/j.chemgeo.2012.06.008
- 828 Christian JW, Mahajan S (1995) Deformation twinning. *Prog Mater Sci* 39:1–157. doi:
829 10.1002/pssb.2221910204
- 830 Clark BR, Kelly WC (1973a) Sulfide Deformation Studies; I, Experimental deformation of
831 pyrrhotite and sphalerite to 2,000 bars and 500 degrees C. *Econ Geol* 68:332–352. doi:

- 832 10.2113/gsecongeo.68.3.332
- 833 Clark BR, Kelly WC (1973b) Sulfide deformation studies; I, experimental deformation of
834 pyrrhotite and sphalerite to 2,000 Bars and 500 degrees C. *Econ Geol* 68:332–352. doi:
835 10.2113/gsecongeo.68.3.332
- 836 Clerc C, Lahfid A, Monié P, Lagabrielle Y, Chopin C, Poujol M, Boulvais P, Ringenbach JC,
837 Masini E, De St Blanquat M (2015) High-temperature metamorphism during extreme
838 thinning of the continental crust: A reappraisal of the North Pyrenean passive
839 paleomargin. *Solid Earth* 6:643–668. doi: 10.5194/se-6-643-2015
- 840 Cochelin B, Lemirre B, Denèle Y, De Saint Blanquat M, Lahfid A, Duchêne S (2017)
841 Structural inheritance in the Central Pyrenees : the Variscan to Alpine
842 tectonometamorphic evolution of the Axial Zone. *J Geol Soc London* 175:336–351. doi:
843 <https://doi.org/10.1144/jgs2017-066>
- 844 Cook NJ, Ciobanu CL, Pring A, Skinner W, Shimizu M, Danyushevsky L, Saini-Eidukat B,
845 Melcher F (2009) Trace and minor elements in sphalerite: A LA-ICPMS study. *Geochim*
846 *Cosmochim Acta* 73:4761–4791. doi: 10.1016/j.gca.2009.05.045
- 847 Couderc J, Dudouit I, Hennig-Michaeli C, Levade C (1985) The interaction between slip and
848 twinning systems in natural sphalerite experimentally deformed. *Phys Status Solidi*
849 90:581–593. doi: 10.1002/pssa.2210900222
- 850 Cox SF (1987) Flow mechanisms in sulphide minerals. *Ore Geol Rev* 2:133–171
- 851 Cox SF, Etheridge MA (1984) Deformation microfabric development in chalcopyrite in fault
852 zones, Mt. Lyell, Tasmania. *J Struct Geol* 6:167–182. doi: 10.1016/0191-
853 8141(84)90094-4
- 854 Cugerone A (2019) Impact of recrystallization and metamorphism on the mobility of
855 germanium and related elements in orogenic Pb-Zn deposits: example of the Pyrenean
856 Axial Zone mineralizations (France -Spain). PhD thesis Univ Montpellier 1–508

- 857 Cugerone A, Cenki-Tok B, Chauvet A, Le Goff E, Bailly L, Alard O, Allard M (2018a)
858 Relationships between the occurrence of accessory Ge-minerals and sphalerite in
859 Variscan Pb-Zn deposits of the Bossost anticlinorium, French Pyrenean Axial Zone:
860 Chemistry, microstructures and ore-deposit setting. *Ore Geol Rev* 95:1–19. doi:
861 10.1016/j.oregeorev.2018.02.016
- 862 Cugerone A, Cenki-Tok B, Muñoz M, Kouzmanov K, Oliot E, Motto-Ros V, Le Goff E
863 (2021a) Behavior of critical metals in metamorphosed Pb-Zn ore deposits: example from
864 the Pyrenean Axial Zone. *Miner Depos* 56:. doi: 10.1007/s00126-020-01000-9
- 865 Cugerone A, Cenki-tok B, Oliot E, Muñoz M, Barou F, Motto-Ros V, Le Goff E (2020)
866 Redistribution of germanium during dynamic recrystallization of sphalerite. *Geology*
867 48:236–241. doi: 10.1130/G46791.1
- 868 Cugerone A, Cenki B, Oliot E, Muñoz M (2023) Structure and texture of Pb-Zn
869 mineralization : example of a multiscale study in the Pyrenees to constrain ore- forming
870 processes and critical metals mobility. *ISTE-WILEY-Science Encycl*. doi:
871 10.51926/ISTE.9124.ch2
- 872 Cugerone A, Oliot E, Chauvet A, Gavaldà Bordes J, Laurent A, Le Goff E, Cenki-Tok B
873 (2018b) Structural Control on the Formation of Pb-Zn Deposits: An Example from the
874 Pyrenean Axial Zone. *Minerals* 8:1–20. doi: 10.3390/min8110489
- 875 Cugerone A, Roger F, Cenki B, Oliot E, Paquette JL (2021b) Variscan U-Th-Pb age for
876 stratabound Pb-Zn mineralization in the Bossòst dome (Pyrenean Axial Zone). *Ore Geol*
877 *Rev* 139, Part:1–18. doi: 10.1016/j.oregeorev.2021.104503
- 878 Di Benedetto F, Bernardini GP, Costagliola P, Plant D, Vaughan DJ (2005) Compositional
879 zoning in sphalerite crystals. *Am Mineral* 90:1384–1392. doi: 10.2138/am.2005.1754
- 880 Drury MR, Urai JL (1990) Deformation-related recrystallization processes. *Tectonophysics*
881 172:235–253. doi: 10.1109/IMFEDK.2013.6602261

- 882 European Commission JRC (2020) Critical materials for strategic technologies and sectors in
883 the EU – A foresight study
- 884 Fleet ME (1983) Investigation of phase transition of natural ZnS minerals by high resolution
885 electron microscopy : discussion. *Am Mineral* 68:845–846
- 886 Fougrouse D, Cugerone A, Reddy SM, Luo K, Motto-ros V (2023) Nanoscale distribution of
887 Ge in Cu-rich sphalerite. *Geochim Cosmochim Acta* 346:223–230. doi:
888 10.1016/j.gca.2023.02.011
- 889 Fougrouse D, Reddy SM, Kirkland CL, Saxey DW, Rickard WD, Hough RM (2019) Time-
890 resolved, defect-hosted, trace element mobility in deformed Witwatersrand pyrite.
891 *Geosci Front* 10:55–63. doi: 10.1016/j.gsf.2018.03.010
- 892 Frenzel M, Hirsch T, Gutzmer J (2016) Gallium, germanium, indium, and other trace and
893 minor elements in sphalerite as a function of deposit type - A meta-analysis. *Ore Geol*
894 *Rev* 76:52–78. doi: 10.1016/j.oregeorev.2015.12.017
- 895 García-Sansegundo J, Alonso JL (1989) Stratigraphy and structure of the southeastern Garona
896 Dome. *Geodin Acta* 3:127–134. doi: 10.1080/09853111.1989.11105180
- 897 George LL, Cook NJ, Ciobanu CL (2016) Partitioning of trace elements in co-crystallized
898 sphalerite-galena-chalcopyrite hydrothermal ores. *Ore Geol Rev* 77:97–116. doi:
899 10.1016/j.oregeorev.2016.02.009
- 900 Gill JE (1969) Experimental deformation and annealing of sulfides and interpretation of ore
901 textures. *Econ Geol* 64:500–508. doi: 10.2113/gsecongeo.64.5.500
- 902 Gilligan LB, Marshall B (1987) Textural evidence for remobilization in metamorphic
903 environments. *Ore Geol Rev* 2:205–229. doi: 10.1016/0169-1368(87)90029-1
- 904 Guan D, Rainforth WM, Ma L, Wynne B, Gao J (2017) Twin recrystallization mechanisms
905 and exceptional contribution to texture evolution during annealing in a magnesium alloy.
906 *Acta Mater* 126:132–144. doi: 10.1016/j.actamat.2016.12.058

- 907 Hadadzadeh A, Mokdad F, Wells MA, Chen DL (2018) A new grain orientation spread
908 approach to analyze the dynamic recrystallization behavior of a cast-homogenized Mg-
909 Zn-Zr alloy using electron backscattered diffraction. *Mater Sci Eng A* 709:285–289. doi:
910 10.1016/j.msea.2017.10.062
- 911 Hirth G, Tullis J (1992) Dislocation creep regimes in quartz aggregates. *J Struct Geol* 14:145–
912 159. doi: 10.1016/0191-8141(92)90053-Y
- 913 Johan Z (1988) Indium and germanium in the structure of sphalerite: an example of coupled
914 substitution with copper. *Mineral Petrol* 39:211–229. doi: 10.1007/BF01163036
- 915 Johnson CA, Cardellach E, Tritlla J, Hanan BB (1996) Cierco Pb-Zn-Ag Vein Deposits:
916 Isotopic and Fluid Inclusion Evidence for Formation during the Mesozoic Extension in
917 the Pyrenees of Spain. *Econ Geol* 91:497–506. doi: 10.5962/bhl.title.18736
- 918 Kelly WC, Clark BR (1975) Sulfide deformation studies: III. experimental deformation of
919 chalcopyrite to 2,000 bars and 500°C. *Econ Geol* 70:431–453. doi:
920 10.2113/gsecongeo.70.3.431
- 921 Kollenberg W, Siemes H (1983) Experimental deformation of sphalerite-garnet ore under a
922 confining pressure of 300 MPa and at temperatures between 250° C and 300° C. *Deform*
923 *Multi-Phase Part Contain Mater Mater Sci* (Eds JB Bild N Hansen A Horsewell, T
924 Leffers, H Liholt) 351–356
- 925 Laforet C, Oudin E, Picot P, Pierrot R, Pillard F (1981) Métallogénie régionale: Utilisation
926 des paragenèses minéralogiques et des minéraux traceurs. *Bur Rech Geol Minieres Rapp*
927 80 SGN175:33p.
- 928 Lawrence LJ (1973) Polymetamorphism of the sulphide ores of Broken Hill, NSW, Australia.
929 *Miner Depos* 8:211–236
- 930 Lockington JA, Cook NJ, Ciobanu CL (2014) Trace and minor elements in sphalerite from
931 metamorphosed sulphide deposits. *Mineral Petrol* 108:873–890. doi: 10.1007/s00710-

- 932 014-0346-2
- 933 Luo K, Cugerone A, Zhou M-F, Zhou J-X, Sun G-T, Xu J, He K-J, Lu M-D (2022)
- 934 Germanium enrichment in sphalerite with acicular and euhedral textures: an example
- 935 from the Zhulingou carbonate-hosted Zn(-Ge) deposit, South China. *Miner Depos*. doi:
- 936 10.1007/s00126-022-01112-4
- 937 Mahajan S, Pande CS, Imam MA, Rath BB (1997) Formation of annealing twins. *Acta Mater*
- 938 45:2633–2638
- 939 McCarley J, Tin S (2019) Understanding the effects of recrystallization and strain induced
- 940 boundary migration on $\Sigma 3$ twin boundary formation in Ni-base superalloys during
- 941 iterative sub-solvus annealing. *Mater Sci Eng A* 740–741:427–438. doi:
- 942 10.1016/j.msea.2018.10.013
- 943 Mezger JE, Gerdes A (2016) Early Variscan (Visean) granites in the core of central Pyrenean
- 944 gneiss domes: Implications from laser ablation U-Pb and Th-Pb studies. *Gondwana Res*
- 945 29:181–198. doi: 10.1016/j.gr.2014.11.010
- 946 Muechez P, Heijlen W, Banks D, Blundell D, Boni M, Grandia F (2005) 7: Extensional
- 947 tectonics and the timing and formation of basin-hosted deposits in Europe. *Ore Geol Rev*
- 948 27:241–267. doi: 10.1016/j.oregeorev.2005.07.013
- 949 Munoz M, Baron S, Boucher A, Béziat D, Salvi S (2016) Mesozoic vein-type Pb–Zn
- 950 mineralization in the Pyrenees: Lead isotopic and fluid inclusion evidence from the Les
- 951 Argentières and Lacore deposits. *Comptes Rendus Geosci* 348:322–332. doi:
- 952 10.1016/j.crte.2015.07.001
- 953 Munoz M, Boyce AJ, Courjault-Rade P, Fallick AE, Tollon F (1994) Multi-stage fluid
- 954 incursion in the Palaeozoic basement-hosted Saint-Salvy ore deposit (NW Montagne
- 955 Noire, southern France). *Appl Geochemistry* 9:609–626. doi: 10.1016/0883-
- 956 2927(94)90022-1

- 957 Oudin E, Pouit G, Tollon F (1988) Les minéraux en trace de Ni-Co, Sn, Ge-Ga, Pb-Sb, Ag et
958 Au témoins de l'évolution de l'hydrothermalisme de l'Ordovicien au Dévonien dans les
959 minéralisations zincifères des Pyrénées Centrales. Bull minéralogique 111:49–63
- 960 Paradis S, Petts D, Simandl GJ, Sharpe R, Hamilton TS, Fayek M, Jackson SE (2023) Impact
961 of deformation and metamorphism on sphalerite chemistry – element mapping of
962 sphalerite in carbonate-hosted Zn-Pb sulfide deposits of the Kootenay Arc , southern
963 British Columbia , Canada and northeastern. Ore Geol Rev 105482. doi:
964 10.1016/j.oregeorev.2023.105482
- 965 Pesquera A, Velasco F (1993) Ore Metamorphism in Sulfide Mineralizations from the Cinco
966 Villas Massif (Western Pyrenees, Spain). Econ Geol 88:266–282
- 967 Pesquera A, Velasco F (1989) The arditurri Pb-Zn-F-Ba deposit (Cinco Villas massif, Basque
968 Pyrenees): A deformed and metamorphosed stratiform deposit. Miner Depos 24:199–
969 209. doi: 10.1007/BF00206443
- 970 Piazzolo S, La Fontaine A, Trimby P, Harley S, Yang L, Armstrong R, Cairney JM (2016)
971 Deformation-induced trace element redistribution in zircon revealed using atom probe
972 tomography. Nat Commun 7:10490. doi: 10.1038/ncomms10490
- 973 Plimer IR (1987) Remobilization in high-grade-metamorphic environments. Ore Geol Rev
974 2:231–245
- 975 Pouit G (1986) Les minéralisations Zn-Pb exhalatives sédimentaires de Bentaillou et de l
976 'anticlinorium paléozoïque de Bosost (Pyrénées ariégeoises, France). Chron la Rech
977 minière 485:3–16
- 978 Pring A, Wade B, McFadden A, Lenehan CE, Cook NJ (2020) Coupled substitutions of minor
979 and trace elements in co-existing sphalerite and wurtzite. Minerals 10:. doi:
980 10.3390/min10020147
- 981 Randle V, Davies H, Cross I (2001) Grain boundary misorientation distributions. Curr Opin

- 982 Solid State Mater Sci 5:3–8. doi: 10.1016/S1359-0286(00)00018-8
- 983 Reddy SM, van Riessen A, Saxey DW, Johnson TE, Rickard WDA, Fougere D, Fischer S,
984 Prosa TJ, Rice KP, Reinhard DA, Chen Y, Olson D (2016) Mechanisms of deformation-
985 induced trace element migration in zircon resolved by atom probe and correlative
986 microscopy. *Geochim Cosmochim Acta* 195:158–170. doi: 10.1016/j.gca.2016.09.019
- 987 Reyx J (1973) Relations entre tectonique, métamorphisme de contact et concentrations
988 métalliques dans le secteur des anciennes mines d'Arre et Anglas (Hautes-Pyrénées -
989 Pyrénées atlantiques). Ph D Thesis, Univ Paris VI 83p
- 990 Rui SS, Shang YB, Fan YN, Han QN, Niu LS, Shi HJ, Hashimoto K, Komai N (2018) EBSD
991 analysis of creep deformation induced grain lattice distortion: A new method for creep
992 damage evaluation of austenitic stainless steels. *Mater Sci Eng A* 733:329–337. doi:
993 10.1016/j.msea.2018.07.058
- 994 Shannon R (1976) Revised effective ionic radii and systematic studies of interatomic
995 distances in Halides and Chalcogenides. *Acta cryst* 32:751–767
- 996 Siemes H, Borges B (1979) Experimental deformation of sphalerite single crystals under
997 confining pressures of 3000 and 5000 bars at temperatures between 25°C and 450°C. *N*
998 *Jb Miner Abb* 134:288–304
- 999 Siemes H, Hennig-Michaeli C (1985) Ore Minerals. *Prefer Orientat Deform Met rocks, an*
1000 *Introd to Mod texture Anal* (Ed HR Wenk Acad Press Orlando 335–360
- 1001 Siemes H, Saynisch HJ, Borges B (1973) Experimentelle Verformung von
1002 Zinkblendeeinkristallen bei Raumtemperatur und 5000 bar Manteldruck. *N Jb Miner*
1003 *Abb* 119:65–82
- 1004 Šrot V, Rečnik A, Scheu C, Šturm S, Mirtič B (2003) Stacking faults and twin boundaries in
1005 sphalerite crystals from the Trepca mines in Kosovo. *Am Mineral* 88:1809–1816. doi:
1006 10.2138/am-2003-11-1222

- 1007 Stanton RL, Gorman H (1968) A phenomenological study of grain boundary migration in
1008 some common sulfides. *Econ Geol* 63:907–923. doi: 10.2113/gsecongeo.63.8.907
- 1009 Sun G, Zhou J, Cugerone A, Zhou M, Zhou L (2023) Germanium-rich nanoparticles in Cu-
1010 poor sphalerite : A new mechanism for Ge enrichment. *GSA Bull* 1–15. doi:
1011 10.1130/B37014.1/6040167/b37014.pdf
- 1012 Trap P, Roger F, Cenki-Tok B, Paquette JL (2017) Timing and duration of partial melting and
1013 magmatism in the Variscan Montagne Noire gneiss dome (French Massif Central). *Int J*
1014 *Earth Sci* 106:453–476. doi: 10.1007/s00531-016-1417-x
- 1015 U.S. Geological Survey (2019) Mineral Commodity Summaries 2019
- 1016 Vikentyev I V., Belogub E V., Novoselov KA, Moloshag VP (2016) Metamorphism of
1017 volcanogenic massive sulphide deposits in the Urals. *Ore geology. Ore Geol Rev.* doi:
1018 10.1016/j.oregeorev.2016.10.032
- 1019 Villars P, Calvert LD (1991) Pearson’s handbook of crystallographic data for intermetallic
1020 phases
- 1021 Vukmanovic Z, Reddy SM, Godel B, Barnes SJ, Fiorentini ML, Barnes SJ, Kilburn MR
1022 (2014) Relationship between microstructures and grain-scale trace element distribution
1023 in komatiite-hosted magmatic sulphide ores. *Lithos* 184–187:42–61. doi:
1024 10.1016/j.lithos.2013.10.037
- 1025 Wagner T, Cook NJ (1998) Sphalerite remobilization during multistage hydrothermal
1026 mineralization events —examples from siderite-Pb-Zn-Cu-Sb veins, Rheinisches
1027 Schiefergebirge, Germany. *Mineral Petrol* 63:223–241. doi: 10.1007/BF01164152
- 1028 Walter BF, Gerdes A, Kleinhanns IC, Dunkl I, von Eynatten H, Kreissl S, Markl G (2018)
1029 The connection between hydrothermal fluids, mineralization, tectonics and magmatism
1030 in a continental rift setting: fluorite Sm-Nd and hematite and carbonates U-Pb
1031 geochronology from the Rhinegraben in SW Germany. *Geochim Cosmochim Acta*

- 1032 240:11–42. doi: 10.1016/J.GCA.2018.08.012
- 1033 Ye L, Cook NJ, Ciobanu CL, Yuping L, Qian Z, Tiegeng L, Wei G, Yulong Y,
1034 Danyushevskiy L (2011) Trace and minor elements in sphalerite from base metal
1035 deposits in South China: A LA-ICPMS study. Ore Geol Rev 39:188–217. doi:
1036 10.1016/j.oregeorev.2011.03.001
- 1037 Zwart HJ (1963) The Structural Evolution of the Paleozoic of the Pyrenees. Geol Rundschau
1038 53:170–205
- 1039
- 1040

1041

Figure captions

1042

1043 Figure 1. A. Map of the western-European Variscan craton and location of the study area
1044 (framed in red; modified from Cugerone et al. 2020). B. Simplified geological map of the
1045 Pyrenean Axial Zone (PAZ) and the Montagne Noire massifs, with location of the studied Pb-
1046 Zn deposits. C. Summary of the main characteristics of type (i), (ii), (iii) and (iv) sphalerite.

1047

1048 Figure 2. Oriented polished hand specimens and thin sections scans of studied samples
1049 (abbreviations: Cal-calcite; Chl-chlorite; Gn-galena; Qz-quartz; Sd-siderite; Sp-sphalerite).
1050 All the sample surfaces are oriented perpendicular to the main cleavage, except the sample
1051 from Saint-Salvy (type iii), which is not oriented (E=east; W= west; N=north; S=south); A-B.
1052 Scanned polished sample and reflected light microphotograph (etched with HClO) of type (i)
1053 sphalerite with polygonal grains from the Bentaillou deposit. Millimeter to centimeter size
1054 sphalerite crystals are identified; C-D. Scanned polished sample and transmitted light
1055 microphotograph of type (ii) sphalerite from the Pale Bidau deposit. Light- to dark-brown
1056 millimeter-thick chemical zones (Fe-rich and Fe-poor) are noticed. Figures 6 and 13 are
1057 located, and a white arrow shows the limit of a sphalerite grain in the zoom; E. Scanned
1058 transmitted light microphotograph of type (iii) sphalerite from the Saint-Salvy deposit
1059 composed of euhedral grains with dark-brown zones and rhythmic bands. Location of Figure
1060 7 is mentioned; F. Scanned transmitted light microphotograph of Type (iv) sphalerite from the
1061 Anglas deposit composed of light- to dark-brown domains. Location of the two analyzed
1062 areas of the Figure 9A and 9E is shown; G-H. Scanned polished sample and transmitted light
1063 microphotograph of type (iv) sphalerite from the Arre deposit with light- to dark-brown
1064 domains. The main tectonic cleavage observed in sphalerite (~N100-110) is mentioned with
1065 dashed white lines. A zoom in (G) shows a macroscale example of dark and light-brown

1066 domains and a second zoom in (H) show a microscale view on the color zoning in sphalerite,
1067 overprinted by tectonic cleavage. The location of Figure 10 is shown in (H).

1068

1069 Figure 3. Microstructural characteristics of the four types of sphalerite textures, quantified
1070 with EBSD analyses. A. Idealized 3D model and cross-section parallel to (110) of a
1071 hextetrahedral crystal; B. Box and whisker plots of the grain sizes. Grain size is calculated
1072 with the equivalent circle diameter method. The total EBSD area is the sum of each area
1073 measured for each sphalerite type; C. Grain orientation spread (GOS) compared to grain
1074 population distribution (cumulative) and analyzed surface (mm^2). For each sphalerite crystal,
1075 GOS has been calculated considering twin ($\Sigma 3$) as grain boundaries to prevent misorientation
1076 artefact from 60° twins. Recrystallized (DRX) fraction is generally positively correlated to the
1077 cumulative grain population divided by analyzed surface. Type (iii) and (iv) sphalerite show
1078 low and high GOS threshold, respectively, evidencing the role of intra-granular plastic
1079 deformation on the GOS threshold results. Conversely, type (i) and (ii) sphalerite exhibit
1080 similar GOS threshold; D. Histogram of the aspect ratio according to grain population and the
1081 analyzed surface (mm^2).

1082

1083 Figure 4. Type (i) sphalerite from the Bentailou deposit (step of measurement: $5 \mu\text{m}$). A.
1084 Misorientation boundary EBSD map with location of the three misorientation profiles in (C).
1085 Low quantity of low-angle ($2\text{-}15^\circ$) misorientation boundaries are observed; B. Histogram of
1086 the misorientation angle distribution plotting neighbor-pair (correlated) and random-pair
1087 (uncorrelated) misorientations; C. Four cumulative misorientation profiles in representative
1088 grains; D. Rose diagram representing long axis slope of the sphalerite grains, according to the
1089 horizontal direction in (A). In the calculation of long axis slope, twin boundaries are not
1090 considered as grain boundary to prevent long axis slope artefacts from the twinned crystals. E.

1091 On the left, one point per grain (oppg; excluding twins as grain boundary) pole figure of the
1092 entire area, and on the right, pole figures of two representative sphalerite grains in the area.
1093 Colors refer to the Euler map in the two selected grains.

1094

1095 Figure 5. Type (ii) sphalerite from the Pale Bidau deposit (step of measurement: 1.5 μm). A.
1096 Reflected light microphotograph with no grain boundaries visible. Only fractures or sharp
1097 changes in grain size can be observed after comparison with (B); B. Grain size map (grain
1098 boundaries with $>15^\circ$ misorientation angle) measured with EBSD. C. Grain reference
1099 orientation deviation (GROD) map. The GROD represents the misorientation deviation for
1100 each pixel compared to the mean misorientation deviation of the entire sphalerite grain. In the
1101 GROD calculation, twin boundaries are considered as grain boundaries to exclude their large
1102 misorientation (60°); D. Misorientation boundary EBSD map. Location of three
1103 misorientation profiles shown in (G) with different colors are represented; E. Rose diagram
1104 representing long axis slope of all the sphalerite grains in the map, according to the horizontal
1105 direction in (A). No significant difference between the three grain size domains has been
1106 identified. F. Histogram of the misorientation angle distribution plotting neighbor-pair
1107 (correlated) and random-pair (uncorrelated) misorientations; G. Three cumulative
1108 misorientation profiles, in representative parent grains.

1109

1110 Figure 6. Type (ii) sphalerite from the Pale Bidau deposit (oppg: one point per grain; step of
1111 measurement: 1.5 μm). An all-Euler EBSD map is shown, as well as three contoured pole
1112 figures (one point per grain, excluding twins as grain boundary) of the three areas located in
1113 the corresponding Euler map. On the bottom right of the figure, a pole figure of one
1114 representative sphalerite parent grain, and inverse pole figures of four representative
1115 recrystallized grain are represented, with colors referring to the Euler map.

1116

1117 Figure 7. Type (iii) sphalerite from the Saint-Salvy deposit (step of measurement: 5 μm). A.
1118 Transmitted light microphotograph showing sphalerite with dark-brown zones and rhythmic
1119 banding. Location of the zoom in (E) is represented in the white box; B. Misorientation
1120 boundary EBSD map; C. Histogram of the misorientation angle distribution plotting
1121 neighbor-pair (correlated) and random-pair (uncorrelated) misorientations; D. Grain reference
1122 orientation deviation (GROD) map. The GROD represents the misorientation deviation for
1123 each pixel compared to the mean misorientation deviation of the entire sphalerite grain. In the
1124 GROD calculation, twin boundaries are considered as grain boundaries to exclude their large
1125 misorientation (60°). Two cumulative misorientation profiles reported in (E) are located; E.
1126 Three cumulative misorientation profiles in representative grains. The third profile in dark
1127 orange color is located in the zoom.

1128

1129 Figure 8. Scatter-contoured pole figures of Type (iii) sphalerite from the Saint-Salvy deposit
1130 with corresponding Euler/textural EBSD maps (oppg: one point per grain; excluding twins as
1131 grain boundary). On the left, oppg pole figure and on the right pole figures of two selected
1132 sphalerite grains with colors referring to Euler map.

1133

1134 Figure 9. Type (iv) from the Anglas deposit (step of measurement: 3 μm). A. Transmitted
1135 light microphotograph of the sphalerite area-1; B. Misorientation boundary EBSD map with
1136 presence of deformation-twins (DT); C. Grain reference orientation deviation (GROD) map.
1137 The GROD represents the misorientation deviation for each pixel compared to the mean
1138 misorientation deviation of the entire sphalerite grain. In the GROD calculation, twin
1139 boundaries are considered as grain boundaries to exclude their large misorientation (60°); D.
1140 Textural component map mostly showing intragranular misorientation ($0\text{-}20^\circ$) across a coarse

1141 sphalerite grain from an initial “reference” orientation point (red cross); E. Reflected light
1142 scan of the area-2 with coarse parent grains boundaries ($>15^\circ$) and between them, local
1143 occurrence of recrystallized fraction (DRX); F. Misorientation boundary EBSD map with
1144 presence of deformation-twins (DT). White arrows represent areas where higher proportion of
1145 low-angle misorientation boundaries; G. Grain reference orientation deviation (GROD) map;
1146 H. Textural component map showing intragranular misorientation ($0-20^\circ$) across coarse
1147 sphalerite grain from an initial “reference” orientation point (red cross). ; I. Histogram of the
1148 misorientation angle distribution plotting neighbor-pair (correlated) and random-pair
1149 (uncorrelated) misorientations; J. Three cumulative misorientation profiles for the area-1 and -
1150 2, located in (B) and (F).

1151

1152 Figure 10. Type (iv) from the Arre deposit (step of measurement: $2.5\ \mu\text{m}$). A. Misorientation
1153 boundary EBSD map with presence of growth- and deformation-twins; B. Grain reference
1154 orientation deviation (GROD) map. The GROD represents the misorientation deviation for
1155 each pixel compared to the mean misorientation deviation of the entire sphalerite grain. In the
1156 GROD calculation, twin boundaries are considered as grain boundaries to exclude their large
1157 misorientation (60°); C. Two textural component maps in two coarse grains showing
1158 intragranular misorientation variations ($0-40^\circ$) from two initial “reference” orientation point
1159 (red crosses); D. Histogram of the misorientation angle distribution plotting neighbor-pair
1160 (correlated) and random-pair (uncorrelated) misorientations; E. Two cumulative
1161 misorientation profiles located in (C).

1162

1163 Figure 11. High-precision EBSD map (step of measurement: $0.5\ \mu\text{m}$) of two areas in the type
1164 (iv) sphalerite from the Arre deposit (same sample as in the Figure 10). A. Low-angle
1165 misorientation ($<5^\circ$) EBSD map with grain boundaries ($>15^\circ$) represented with black lines

1166 and twin boundaries (60°) represented with white line. Three misorientation profiles shown in
1167 (C) are located; B. Textural component map showing intragranular misorientation variation
1168 ($0\text{-}10^\circ$) across a coarse sphalerite grain from one initial “reference” orientation point (red
1169 cross). A black arrow on the lower-right, indicates a plumose structure; C. Three
1170 misorientation profiles located in (A); D. Low-angle misorientation ($< 5^\circ$) EBSD map with
1171 grain boundaries ($> 15^\circ$) represented with black lines and twin boundaries (60°) represented
1172 with white line. E. Textural component map showing intragranular misorientation variation
1173 ($0\text{-}20^\circ$) mainly across two sphalerite grains from one initial “reference” orientation point (red
1174 cross). F. Two misorientation profiles located in (D).

1175

1176 Figure 12. Scatter-contoured pole figures, inverse pole figure and cumulative misorientation
1177 profile with corresponding Euler/textural EBSD maps (oppg: one point per grain; excluding
1178 twins as grain boundary) of Type (iv) sphalerite from the Arre deposit with on the top, pole
1179 figures of a sphalerite grain with color corresponding to the textural component map on the
1180 left (initial “reference” orientation point on the red cross) superimposed on an all Euler angle
1181 map. At the bottom left, a cumulative misorientation profile, located on the map above. In the
1182 middle at the bottom, inverse pole figures of three recrystallized grains are shown with color
1183 corresponding to the Euler map on the right.

1184

1185 Figure 13. Microphotographs, LIBS and EBSD grain size maps of the type (ii) sphalerite from
1186 the Pale Bidau deposit. Coarse domains ($> 100 \mu\text{m}$) are reported based on EBSD map and two
1187 rulers below (A) and (C) indicate the scale. A. Transmitted light microphotograph; B. Grain
1188 size map (grain boundaries with $>15^\circ$ misorientation angle) measured with EBSD,
1189 superimposed on a reflected light microphotograph. Location of profile (B) is shown; C.
1190 Elemental profile with Ga and Cu contents based on intensities of LIBS maps data, which

1191 were converted in concentration based on LA-ICP-MS spot analyses. For Ge, LA-ICP-MS
1192 contents were too low to quantify this profile; C-E. LIBS maps of Cu, Ga and Ge.
1193 Representative LA-ICP-MS analyses previously reported in Cugerone et al. 2018a, 2020 are
1194 mentioned.

1195

1196 Figure 14. EBSD and LIBS maps of the type (iii) sphalerite from the Saint-Salvy deposit. A.
1197 Misorientation boundary EBSD map with 4 circles locating four areas of interest: 1-sector
1198 zoning in a dark brown zone; 2-Elongated dark brown zone in a grain boundary; 3-Dark
1199 brown zones in grain, low angle misorientation and twin boundaries; 4-Dark brown zone in
1200 growing crystal edge; B. Transmitted light microphotograph showing chemical zones in
1201 sphalerite, with rhythmic bands (rb) and sector zoning (sz). C-F. LIBS Ge, Cu, Ga and Sb
1202 maps. G. Stacked LIBS maps with red=Cd and green=Fe. Correlated areas where Fe and Cd
1203 are both concentrated appear in yellow (stacked image processed with ImageJ). H. Stacked
1204 LIBS maps with red=Sn and in green=In. Correlated areas where Sn and In are both
1205 concentrated appear in yellow (stacked image processed with ImageJ).

1206

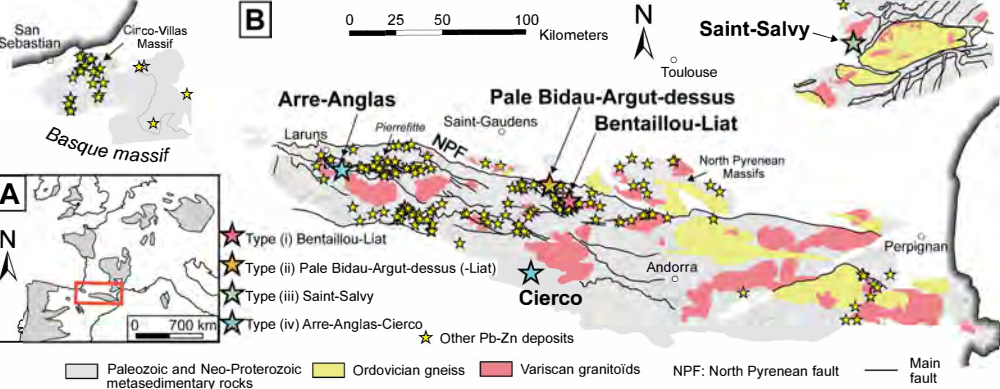
1207 Figure 15. Combined microphotograph, EBSD and LIBS maps of the type (iv) sphalerite from
1208 the Arre deposit. Contours of two coarse parent grains is shown; A. Transmitted light scan
1209 with superimposed low-angle ($<15^\circ$) and high-angle ($>15^\circ$) misorientation boundary maps.
1210 Coarse grains ($> 100 \mu\text{m}$) are light to dark brown colors, but the recrystallized sphalerite is
1211 only light brown; B-C. LIBS Ge and Cu map with four LA-ICP-MS spot analyses reported;
1212 D. Cumulative misorientation profile located in (A-C) in dark and light domain, combined
1213 with Ge and Cu contents, extracted from the LIBS maps. Microscale Ge-minerals observed in
1214 the LIBS maps are evidenced with a yellow circle. Most of Ge and Cu contents are hosted in

1215 nanoscale inclusions of briartite and certainly not in sphalerite lattice (Fougerouse et al.
1216 2023).

1217

1218 Figure 16. Synthesis of the microstructural and trace element distribution in the four types of
1219 sphalerite studied. Macro- and micro-textures are reported at the top of the figure. In the
1220 central part, histograms showing the relative proportion of misorientation boundaries are
1221 represented. Low angle misorientation boundaries (Low mis. in red) as well as specific twin
1222 boundaries such as growth-twins (G.twins in brown), deformation-twins (D.twins in orange)
1223 and annealing-twins (A.twins in blue) are emphasized. At the bottom part of the figure,
1224 microtextural sketches describe the grain size of each sphalerite-type with the various types of
1225 boundaries and simplified representative pole figure of a sphalerite grain. Below, the spatial
1226 distribution of Cu-Ga-Ge at microscale is shown in various tints of blue. Note that rhythmic
1227 bands observed in the type (iii) sphalerite are not limited to a specific crystal compared to
1228 dark-brown zones such as sector zoning. At the bottom, a timescale is proposed with the
1229 various tectonic, hydrothermal and deformation events.

1230

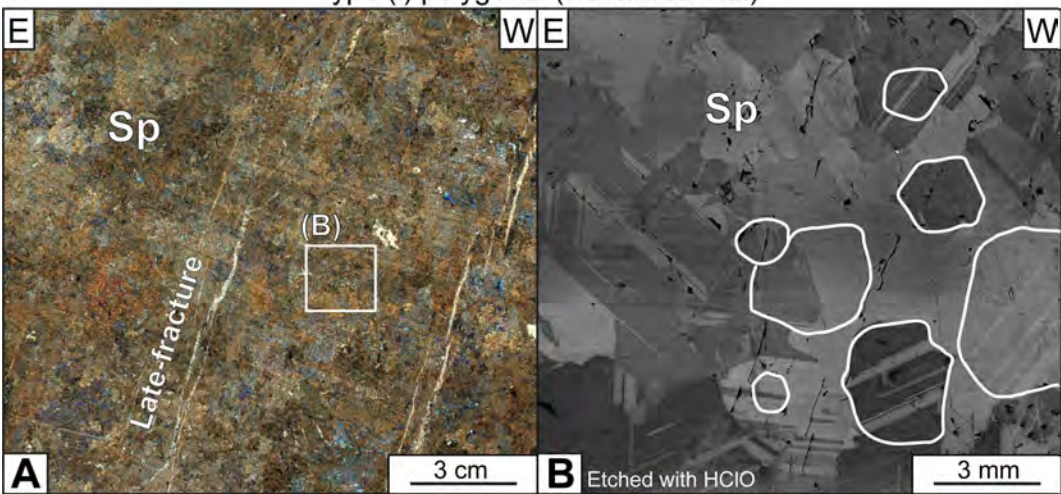


C

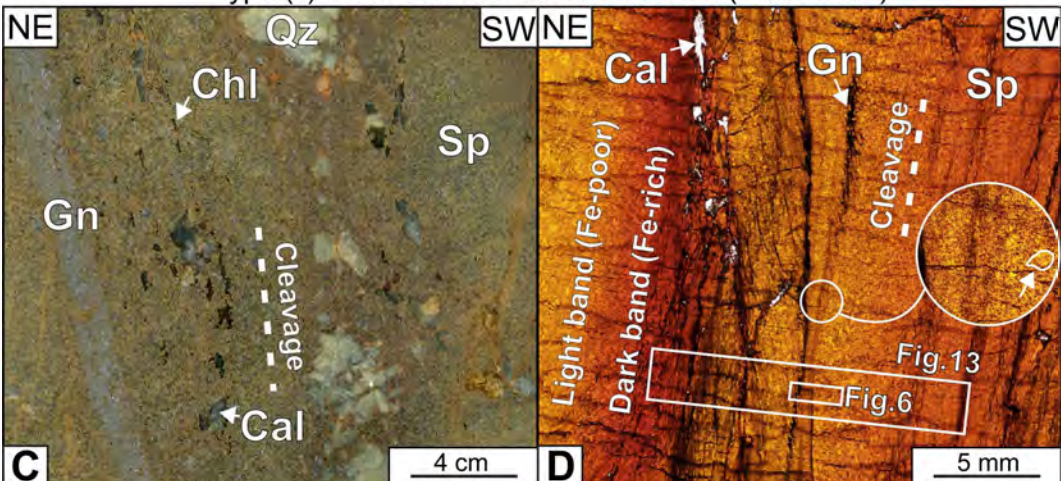
Sphalerite type	Mining district	Ore structure	Ore emplacement	Metamorphism	Sphalerite grain shape/size	Sphalerite color
Type (i)	Bentailou-Liat	Stratabound vein	Variscan	Variscan (300-400 °C)	coarse polygonal (up to ~1-2 mm)	dark-red
Type (ii)	Pale Bidau-Argut-dessus (-Liat)	Crosscutting vein	Late-Variscan	Late-Variscan (< 300 °C)	coarse (~1 mm) to small (~1-2 μm)	dark-red to light-brown
Type (iii)	Saint-Salvy	Crosscutting vein	Mesozoic	poorly metamorphosed	coarse euhedral (up to ~1-2 mm)	dark-brown to light-brown
Type (iv)	Arre-Anglas-Cierco	Crosscutting vein	Post-Variscan (Mesozoic?)	Pyrenean-Alpine (< 300 °C)	coarse (~1 mm) to small (~1-2 μm)	dark-brown to light-brown

Figure 1

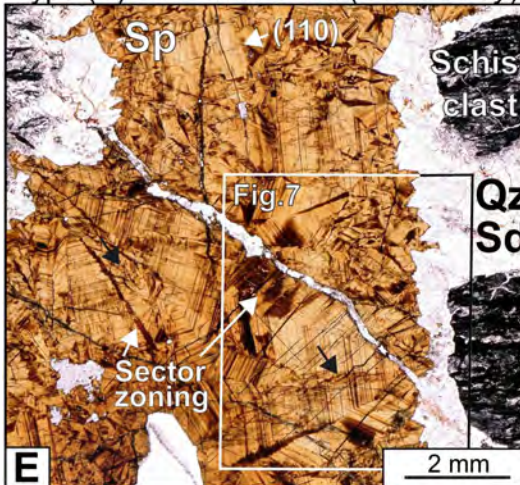
Type (i) polygonal (*Bentallou-Liat*)



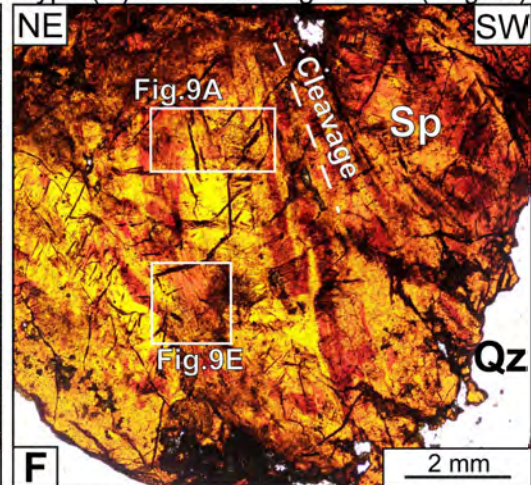
Type (ii) deformed with chemical bands (*Pale Bidau*)



Type (iii) euhedral zoned (*Saint-Salvy*)



Type (iv) deformed dark-light dom. (*Anglas*)



Type (iv) deformed dark-light domains (*Arre*)

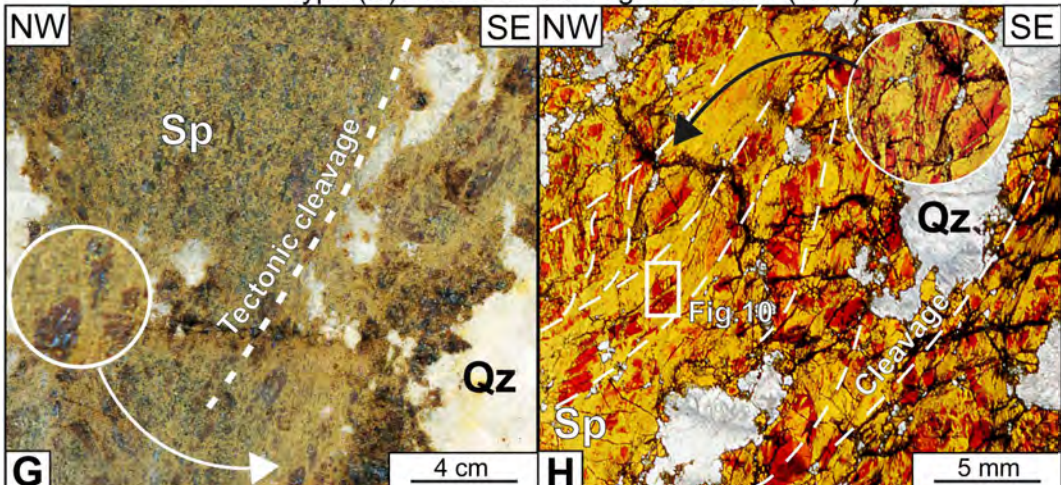


Figure 2

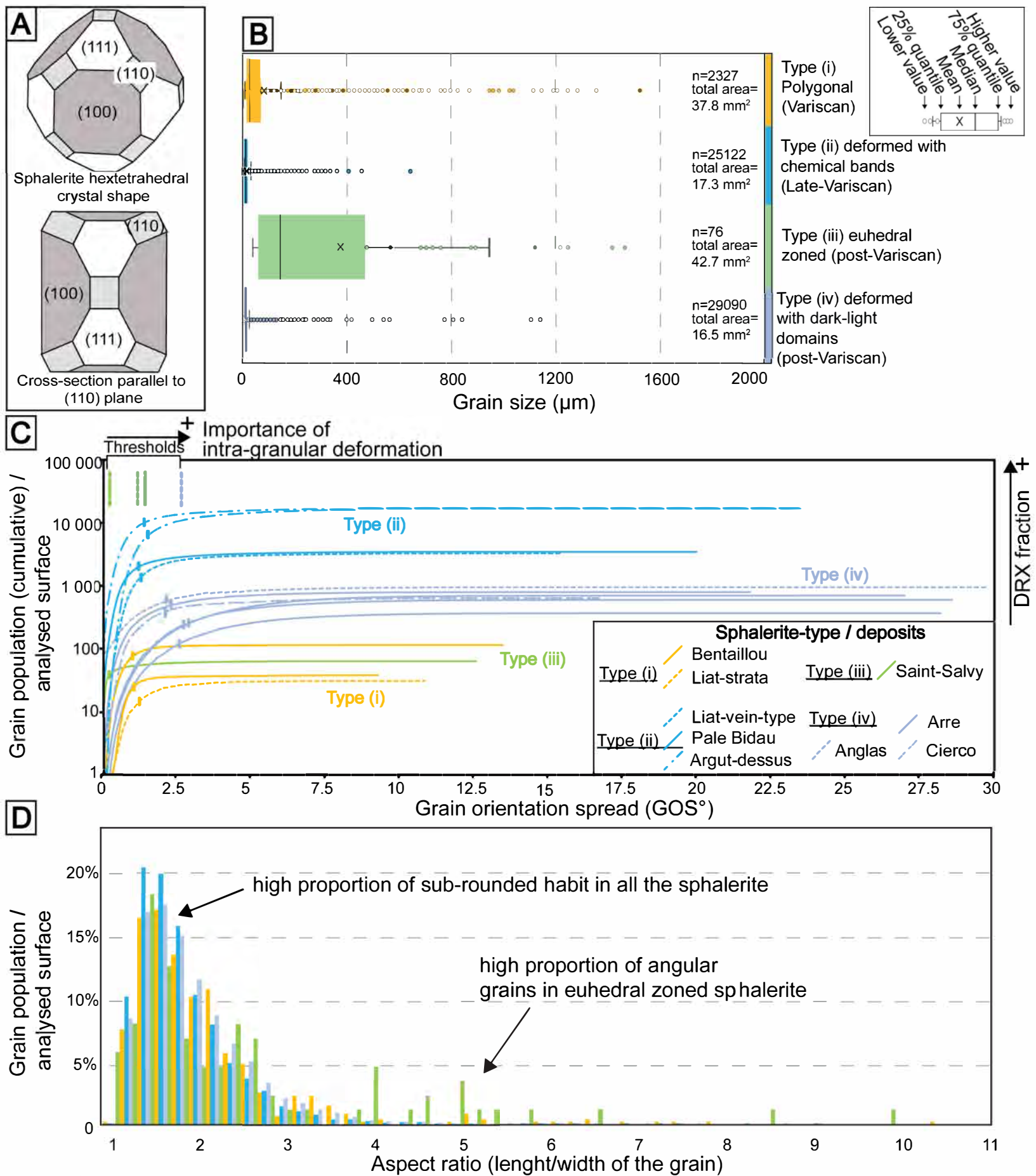


Figure 3

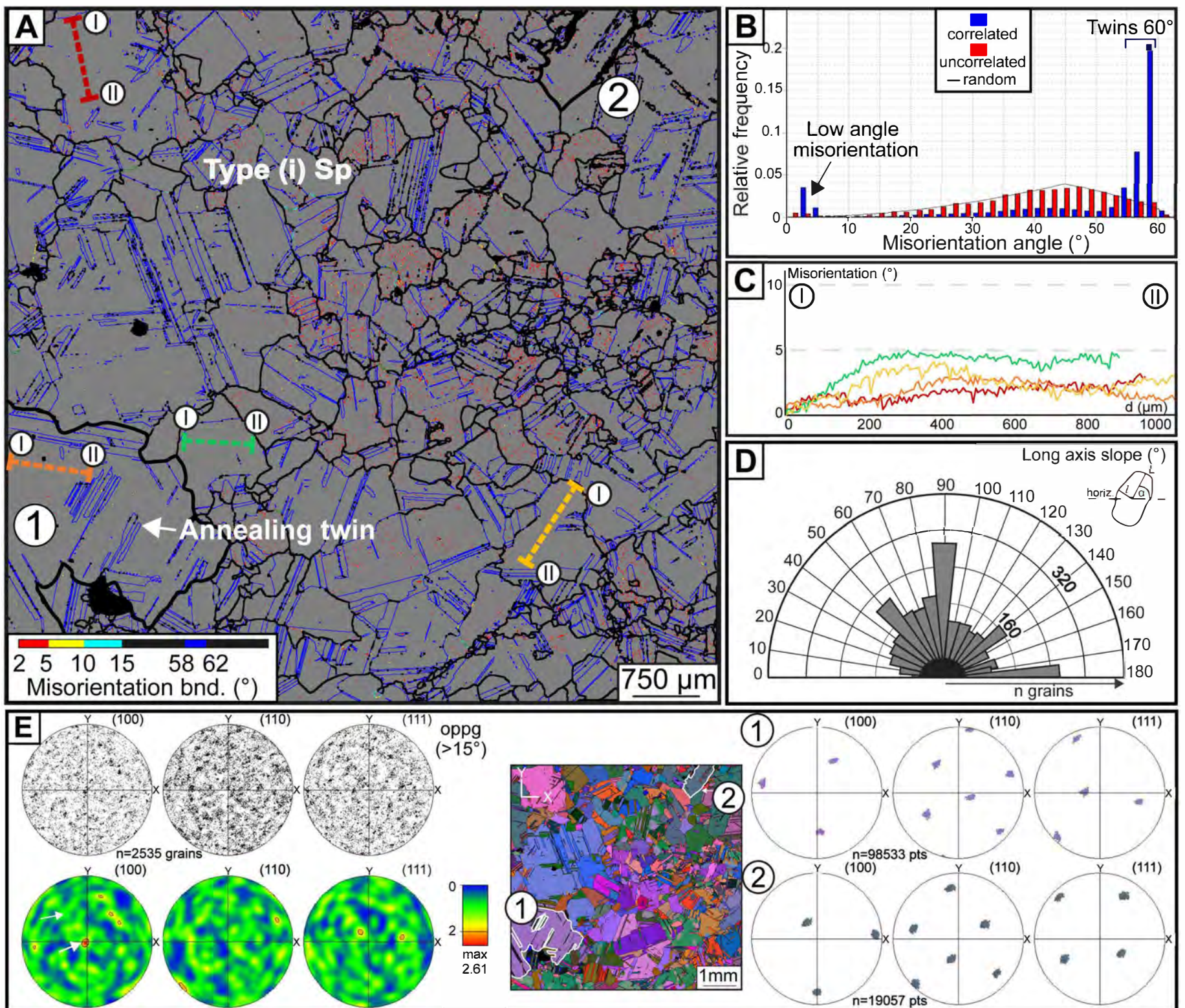


Figure 4

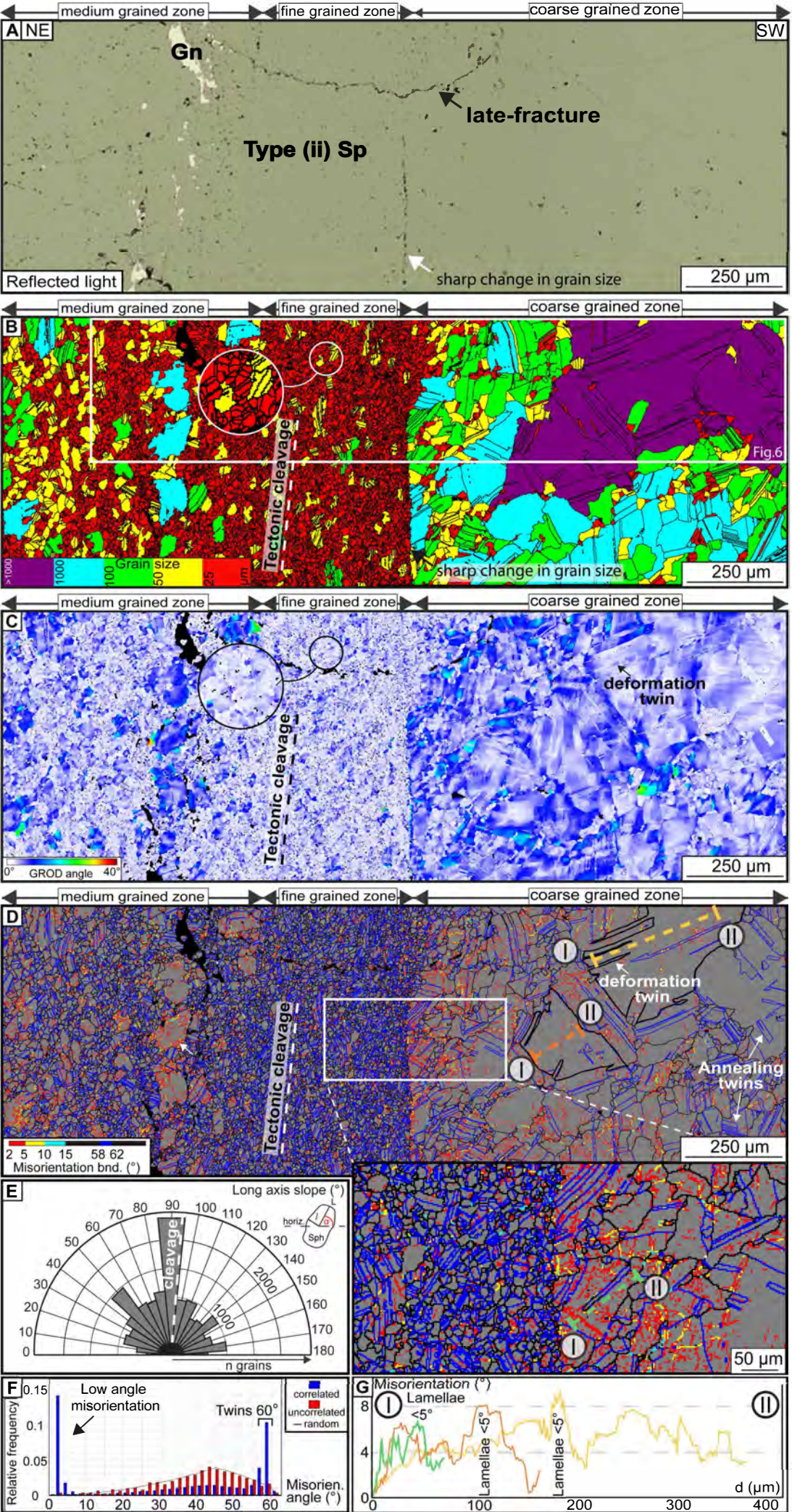


Figure 5

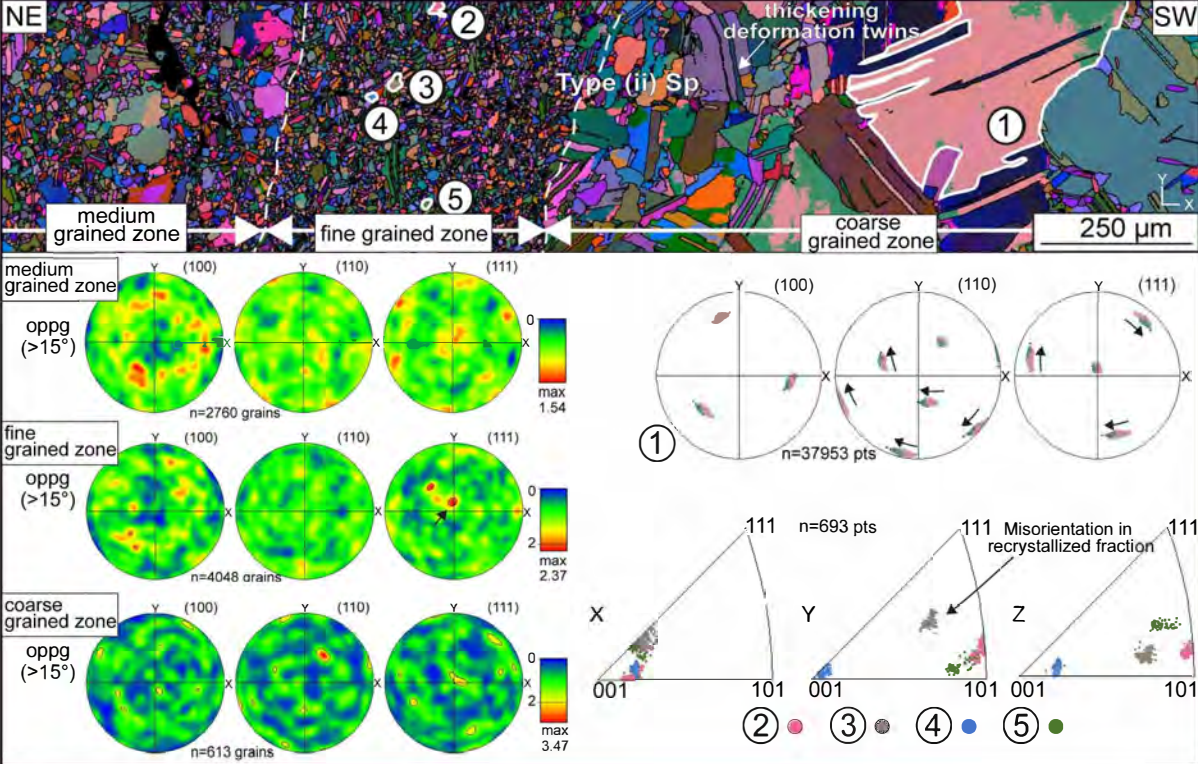


Figure 6

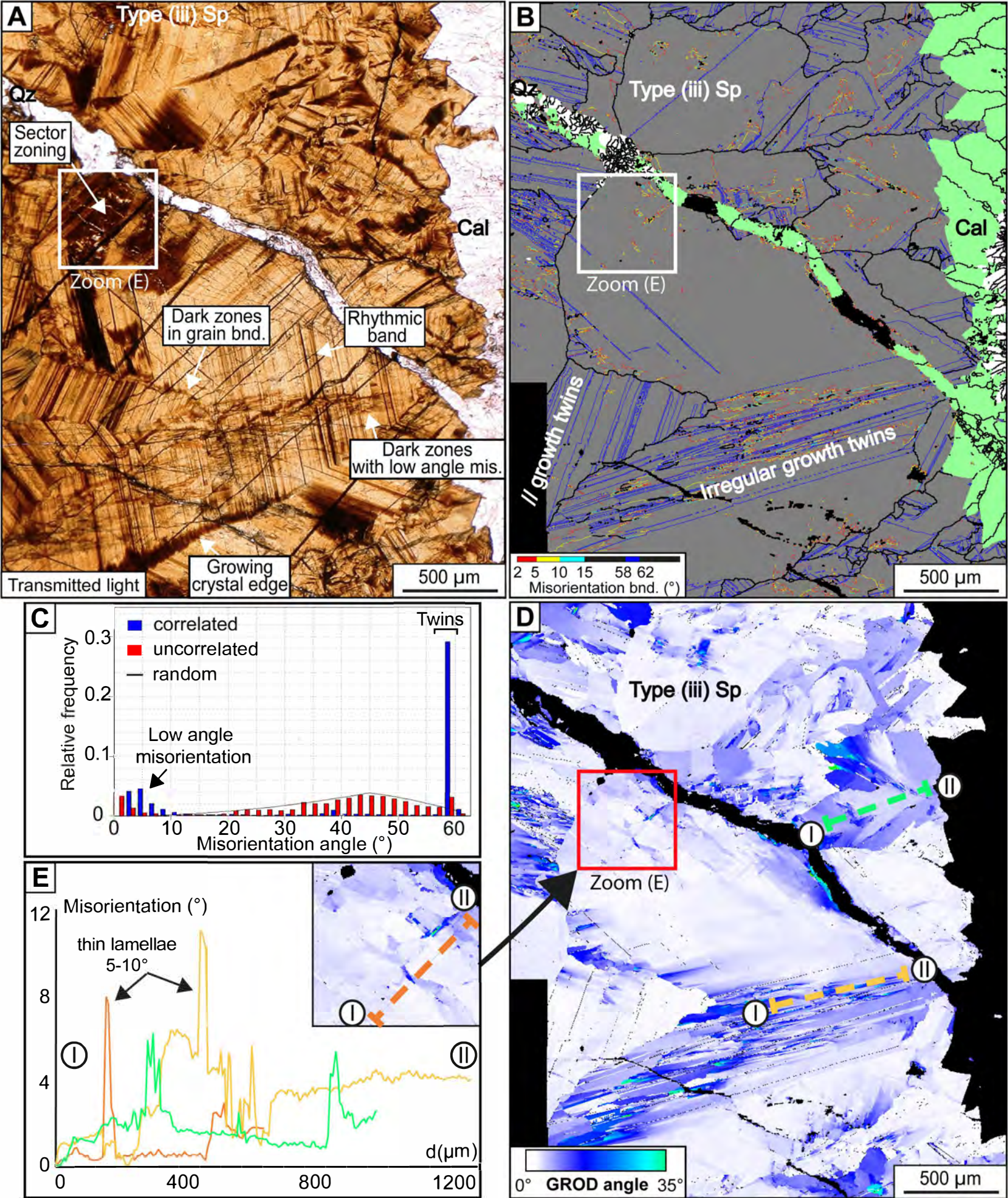


Figure 7

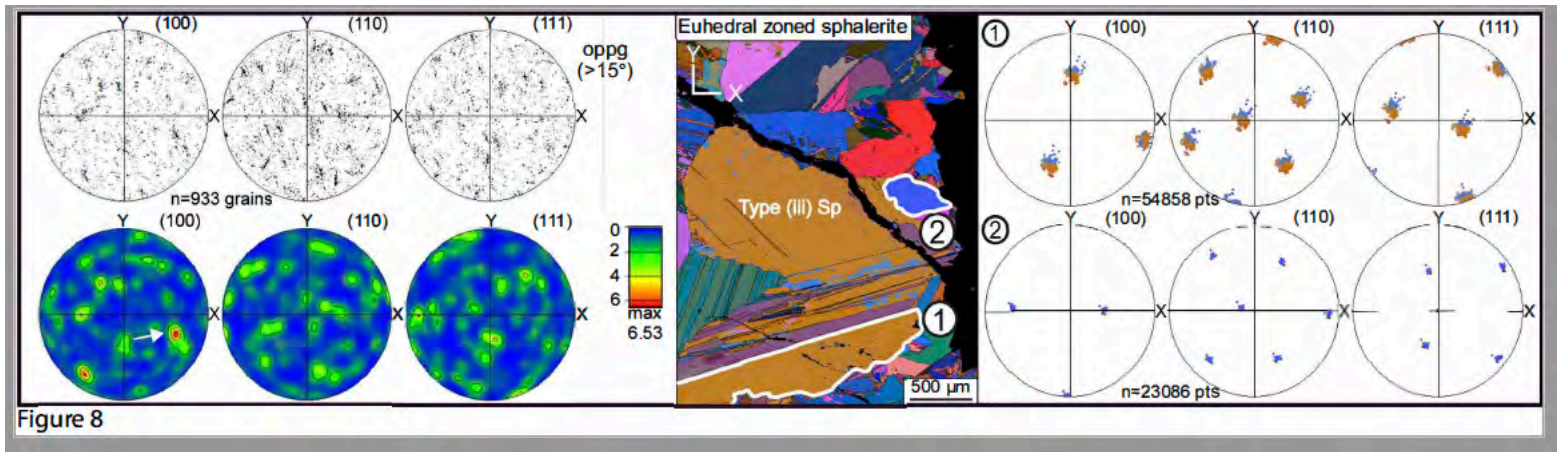


Figure 8

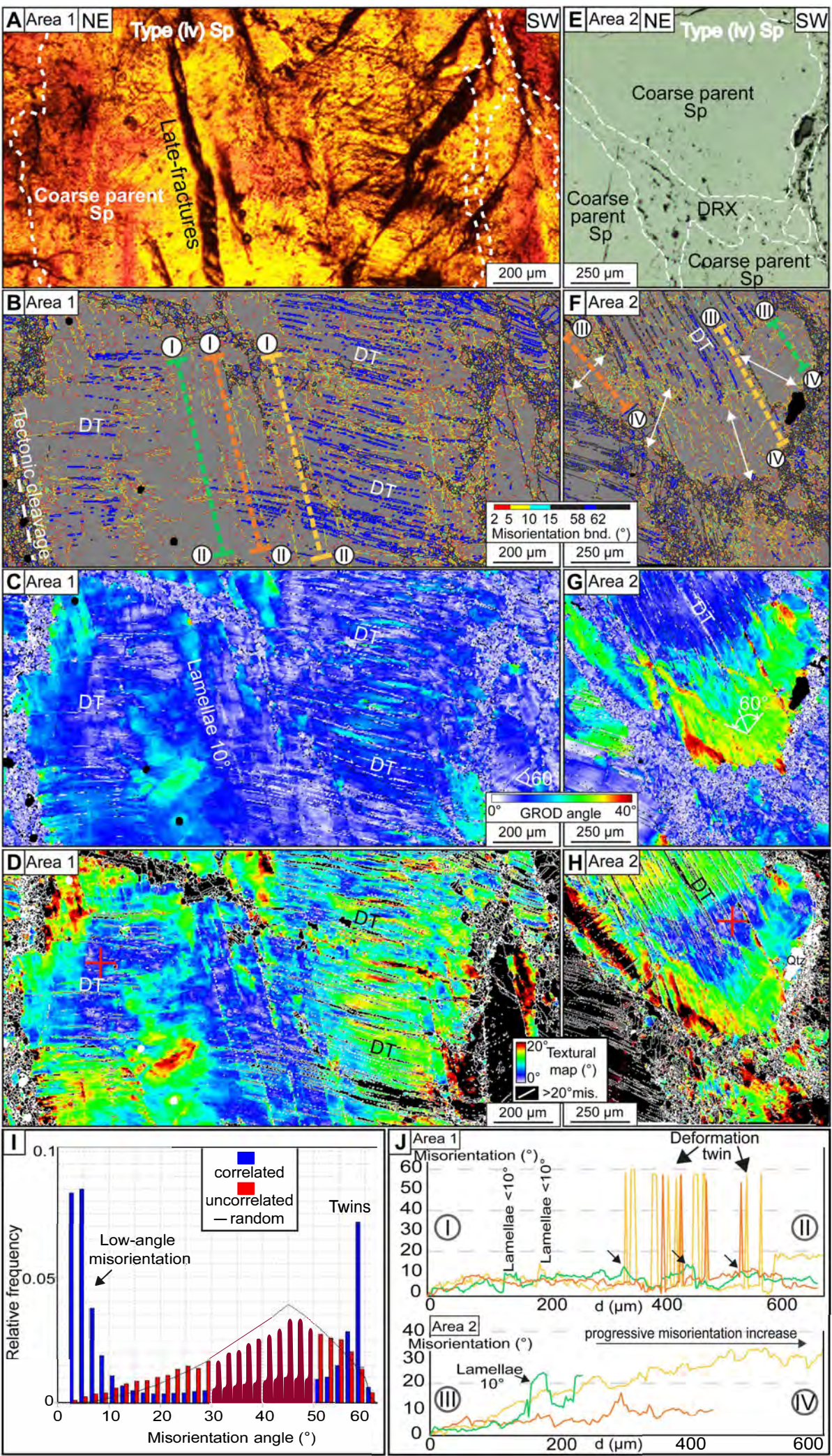


Figure 9

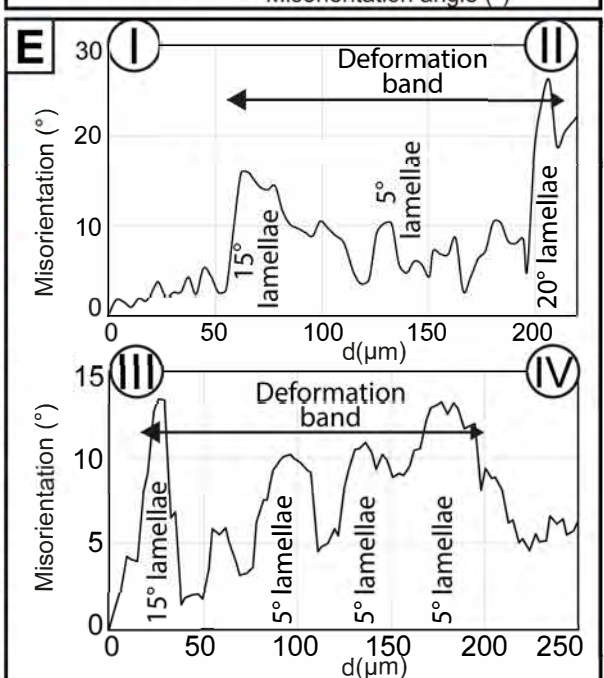
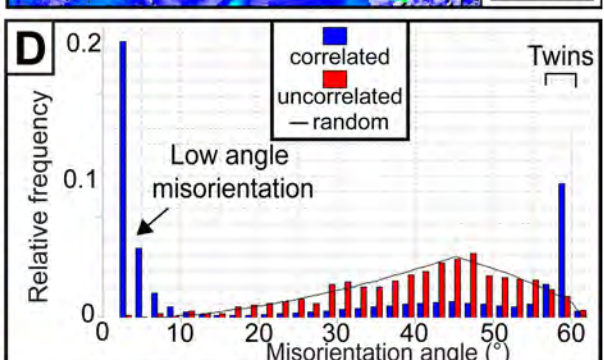
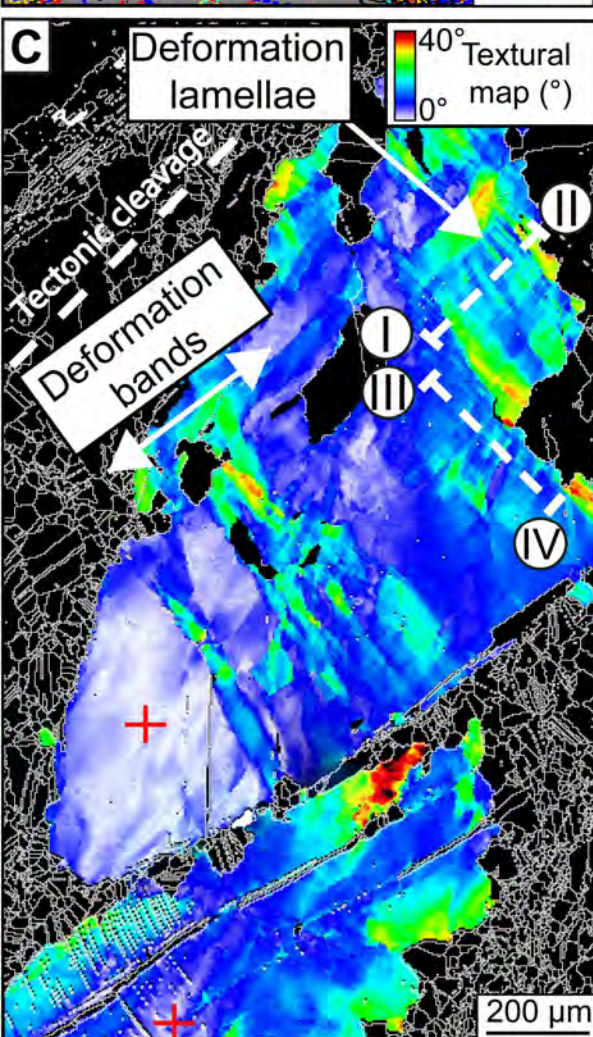
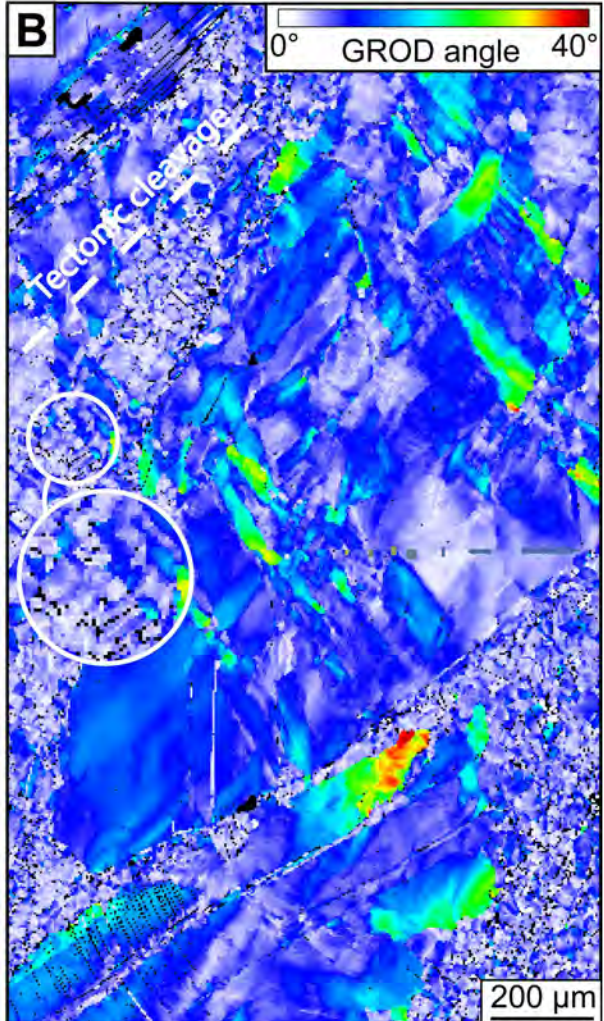
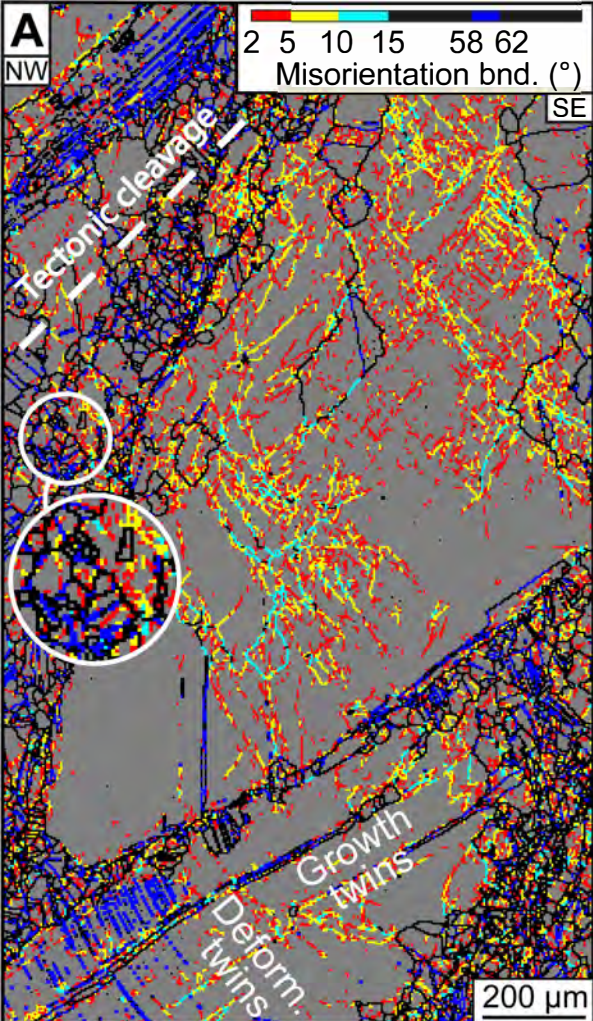


Figure 10

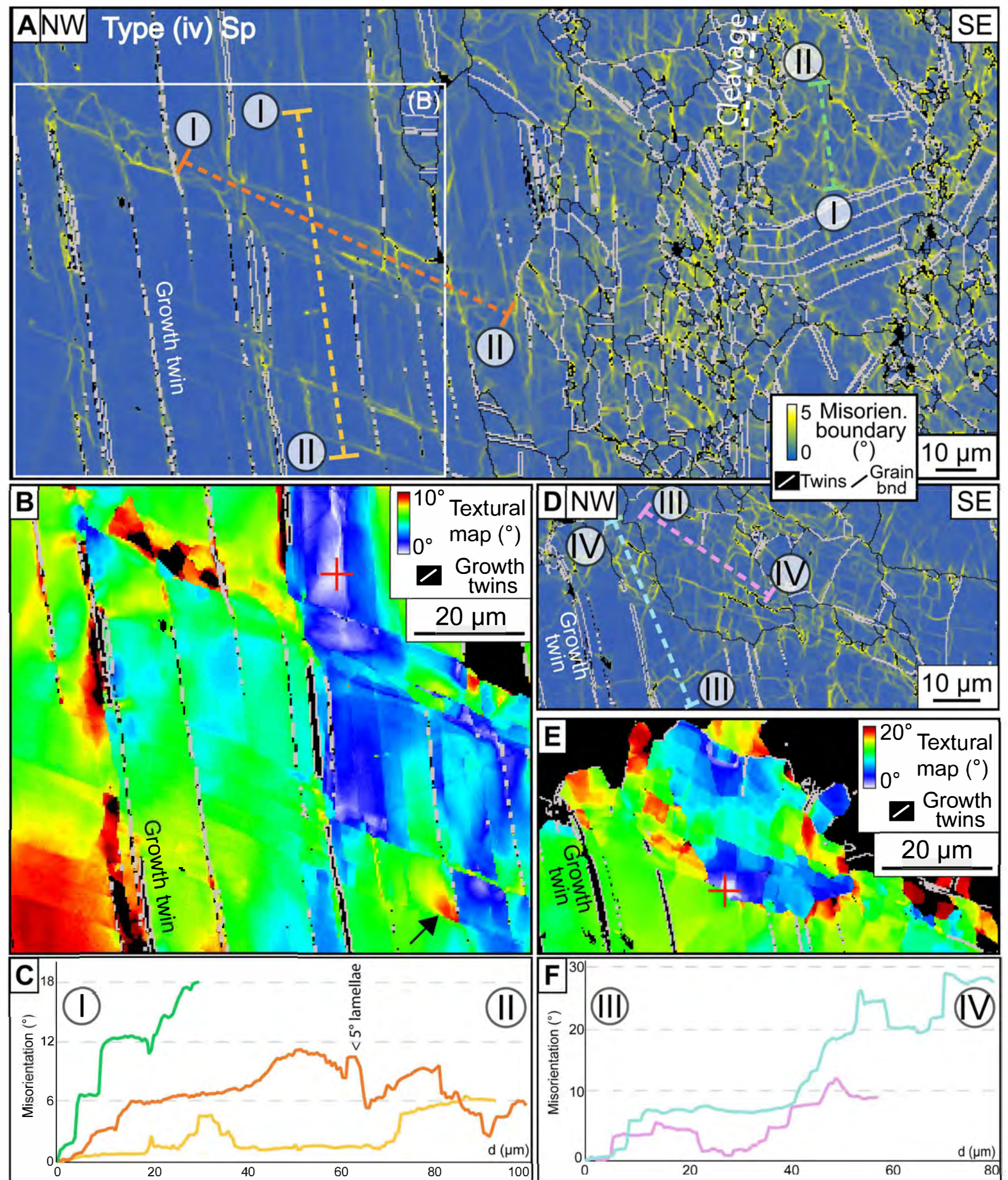


Figure 11

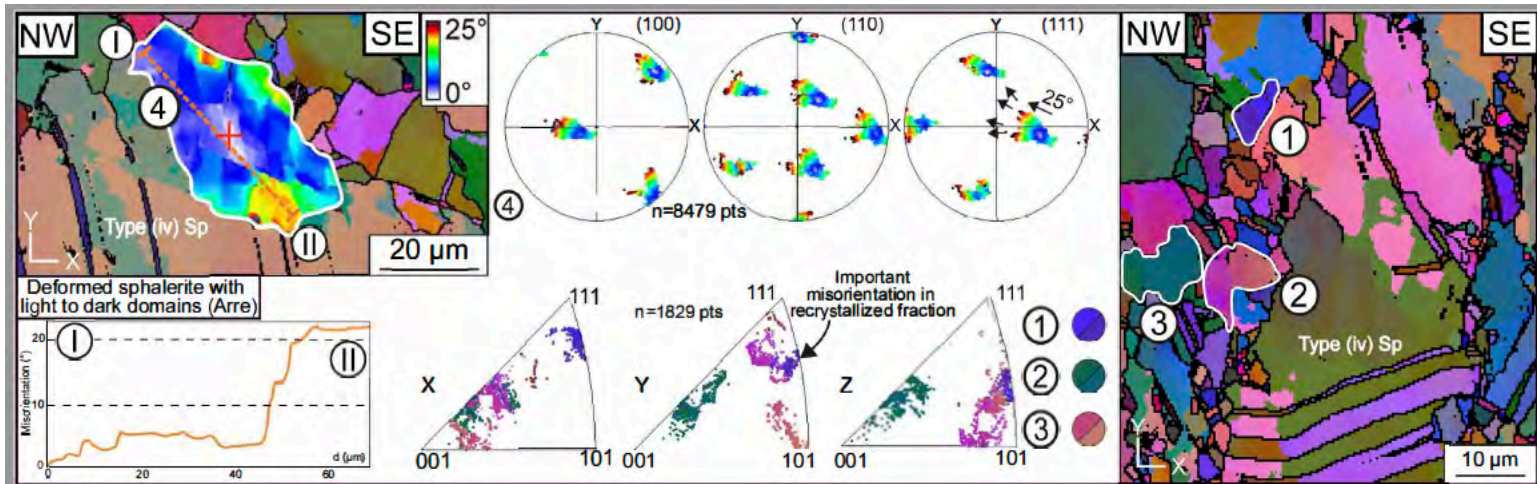


Figure 12

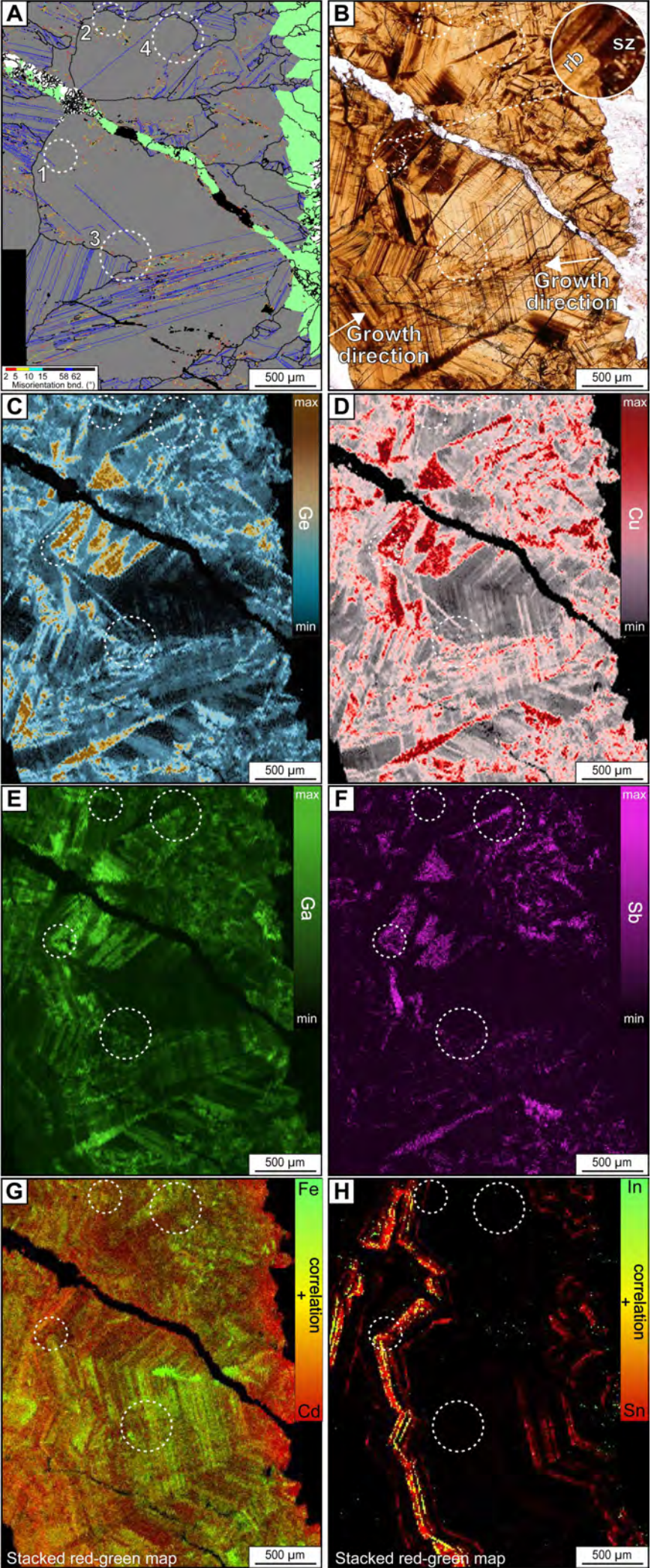


Figure 14

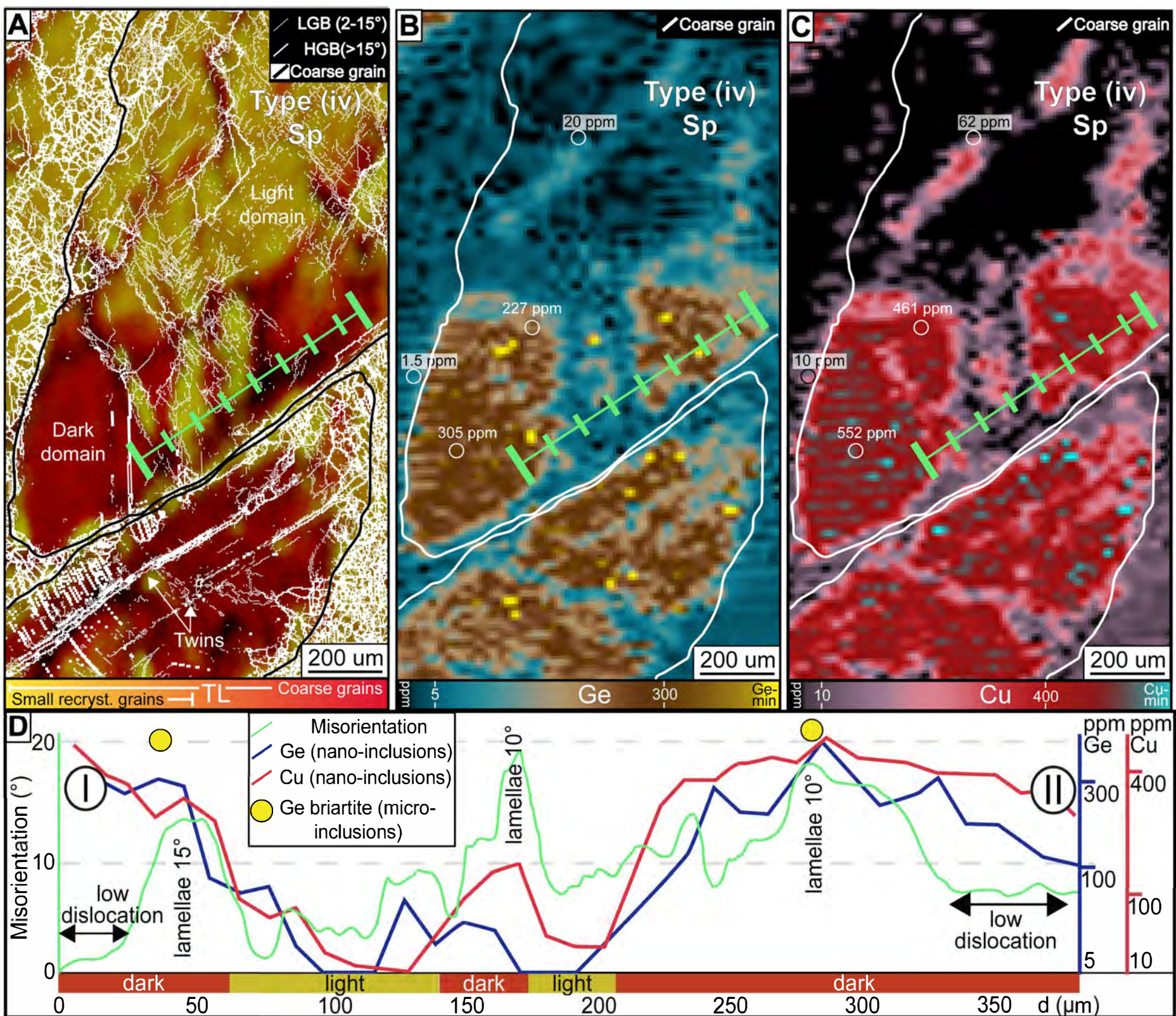


Figure 15

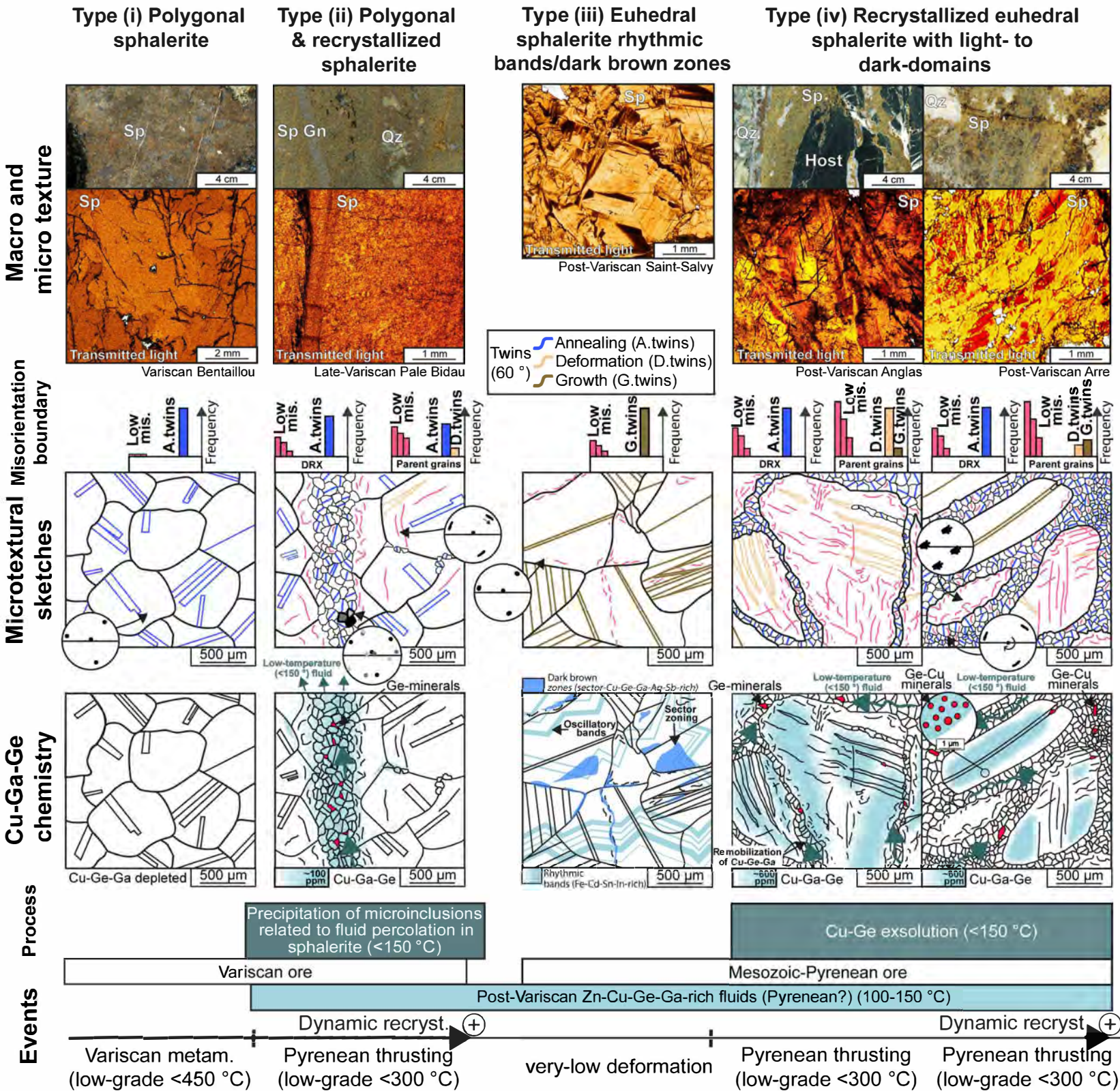


Figure 16